J. Phys.: Condens. Matter **8** (1996) 10049–10082. Printed in the UK

The pseudogap state in high-T_c superconductors: an infrared study

A V Puchkov†, D N Basov‡ and T Timusk†

† Department of Physics and Astronomy, McMaster University, Hamilton, Ontario, Canada L8S 4M1

‡ Department of Physics, Brookhaven National Laboratory, Upton, NY 11973-5000, USA

Received 17 September 1996

Abstract. We report on a study of the electromagnetic response of three different families of high-T_c superconductors that in combination allowed us to cover the whole doping range from under- to overdoped. The discussion is focused on the *ab*-plane charge dynamics in the *pseudogap state* which is realized in underdoped materials below a characteristic temperature T^*, a temperature that can significantly exceed the superconducting transition temperature T_c. We explore the evolution of the pseudogap response by changing the doping level, by varying the temperature from above to below T^*, or by introducing impurities in the underdoped compounds. We employ a memory function analysis of the *ab*-plane optical data that allows us to observe the effect of the pseudogap most clearly. We compare the infrared data with other experimental results, including the *c*-axis optical response, dc transport, and angle-resolved photoemission.

1. Introduction

There is mounting evidence that the normal state of underdoped high-T_c superconductors (HTSC) is dominated by a pseudogap. A number of physical probes show that below a characteristic temperature T^*, which can be well above the superconducting transition temperature T_c, the physical response of HTSC materials can be interpreted in terms of the formation of a partial gap or a pseudogap by which we mean a suppression of the density of low-energy excitations. This gap persists in the superconducting state. T^* decreases with increasing doping in the underdoped regime and since T_c rises with doping, the two curves meet at the optimal doping level, as shown in the schematic phase diagram in figure 1.

The earliest experiments to reveal gap-like behaviour in the normal state were nuclear magnetic resonance (NMR) measurements of the Knight shift [1, 2], which probes the uniform spin susceptibility. In conventional superconductors and the cuprates at optimal doping, the Knight shift is temperature independent in the normal state but drops rapidly below T_c due to pairing of electronic spins into (singlet) superconducting Cooper pairs. In underdoped cuprates, however, the Knight shift begins to drop well above the superconducting transition temperature. Warren *et al* concluded that in these materials spin pairing takes place well above the bulk superconducting transition at T_c, thus producing a normal-state energy gap, referred to as a 'spin gap' [1].

Deviations from the well known linear temperature dependence of the *ab*-plane resistivity [3], $\rho_{ab}(T)$, were observed in underdoped cuprates as well [4–7], with the slope of $\rho_{ab}(T)$ changing below a characteristic temperature T^*. As the doping is increased

0953-8984/96/4810049+34$19.50

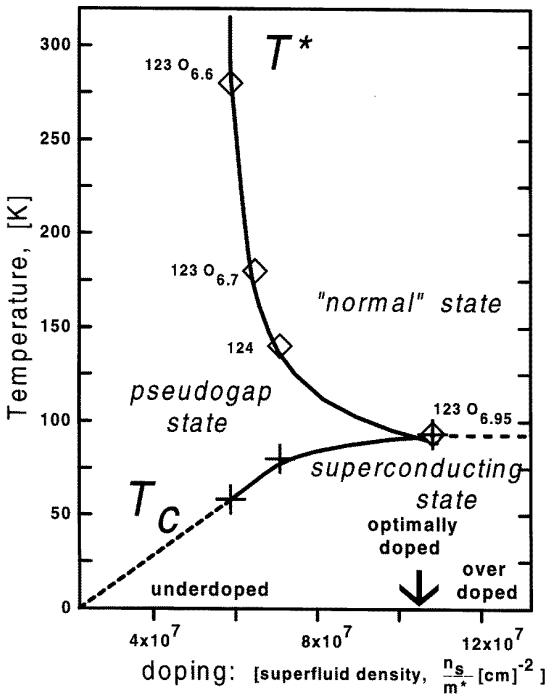

Figure 1. A schematic phase diagram of the cuprate superconductors. In the underdoped regime a pseudogap state forms below a temperature $T^* > T_c$. The curves for T^* and T_c cross at optimal doping where the pseudogap and the superconducting gap develop at the same temperature. T^* is determined from the c-axis conductivity and the doping level from the superfluid density $\omega_{ps}^2 = n_s/m^*$ in the CuO_2 planes.

towards the optimal level, T^* decreases and the near-optimal doping $\rho_{ab}(T)$ is linear over the range of temperatures from T_c to above 800 K [6, 5].

The magnitude of T^* as well as its variation with doping suggest that the suppression of the spin susceptibility observed in NMR measurements and the change of slope of $\rho_{ab}(T)$ have a common physical origin. It has been suggested that if the scattering responsible for the linear temperature dependence of $\rho_{ab}(T)$ involves scattering on spin fluctuations, then the spin gap seen in NMR below T^* would naturally account for the depression of $\rho_{ab}(T)$ below T^* as well. Similar evidence for the suppression of the spin susceptibility has been extracted from neutron scattering experimental results [8]. Specific heat measurements on underdoped $YBa_2Cu_3O_x$ (Y123), however, show that there is a large decrease in entropy below a temperature, closely related to the T^*, which cannot be accounted for by assuming that a gap in the spin degrees of freedom is solely responsible [9].

There is spectroscopic evidence of anomalies in the properties of HTSC that were originally associated with the formation of the superconducting gap, but were found to occur at $T > T_c$ in underdoped samples. The shift in the position and width of Raman frequencies of certain phonons, associated with the onset of superconductivity [10], were shown to occur in the normal state of underdoped cuprates and it was suggested they were related to the spin gap [11]. Similarly, broad peaks in the electronic Raman continuum, also interpreted as an evidence for the formation of a superconducting gap [12], were found

to occur well above T_c in underdoped samples [13].

Indications of normal-state, gap-like anomalies in underdoped cuprates were observed in infrared optical measurements as well. To a first approximation the *ab*-plane optical properties of HTSC are those of a metal where the charge carriers move coherently through the lattice. Such coherent motion gives rise to a conductivity peak, centred at zero frequency, called the Drude peak, whose width is a measure of the inverse lifetime of the carriers. In this paper we call systems that have a conductivity peak at zero frequency coherent systems. In contrast, transport in the *c*-axis direction does not show a peak a zero frequency and we call this incoherent transport. On closer examination the reflectance of most high-temperature superconductors was found to deviate from simple Drude behaviour which predicts a reflectance decreasing monotonically with frequency. A structure in the form of a 'knee' was found at approximately 500 cm^{-1}. This structure was sometimes interpreted as a manifestation of a conventional superconducting gap. It has been found, however, that in underdoped materials the knee starts to develop already in the normal state [14–21]. A comparison with other probes suggests that the knee structure and deviations observed in the dc transport and NMR experiments all occur at a characteristic temperature remarkably similar to T^*. The corresponding changes in the complex optical conductivity $\sigma(\omega) = \sigma_1(\omega) + i\sigma_2(\omega)$ involve a shift of part of the $\sigma_1(\omega)$ spectral weight from 300–700 cm^{-1} to *lower* frequencies, resulting in a marked narrowing of the Drude peak. This behaviour is in accord with decreasing dc resistivity and was interpreted in terms of coupling of electrons to the longitudinal optical (LO) phonons [22, 23] or as a manifestation of the spin gap [16, 20, 21].

It should be emphasized that in the case of a *coherent* system, such as the underdoped cuprates in the *ab*-plane direction, there is no direct mapping between the electronic density of states (DOS) and the shape of the real part of the conductivity, $\sigma_1(\omega)$. For example, even if there is a gap in the electronic DOS and its magnitude is larger than the characteristic energy associated with the *elastic* scattering (clean limit [17, 24]), the gap will not manifest itself in the $\sigma_1(\omega)$ spectra. In the same way, a pseudogap in the electronic DOS of a coherent system, that may appear due to strong interactions in the system, does not appear as an obvious gap in the conductivity.

The charge dynamics along the interplane *c*-direction is *incoherent*, at least in the underdoped materials. While both underdoped Y123 and $YBa_2Cu_4O_8$ (Y124) compounds, collectively referred as YBCO, exhibit a gap-like depression in the *c*-axis conductivity as well [25–27], the *c*-axis conductivity shows no coherent peak at low frequencies; see figure 2. In contrast to the *ab*-plane response, as the temperature decreases from 300 K to T_c the *c*-axis $\sigma_1(\omega)$ spectral weight is transferred from the gap region to *higher* frequencies [25, 28]. This is inferred from the sum rule for the optical conductivity, or spectral weight. The spectral weight lost at low frequency, as the gap develops, does not go to low frequencies since the magnitude of the low-frequency conductivity is in good agreement with the dc resistivity [29] which shows a 'semiconducting' behaviour (i.e. resistivity increases at low T). Thus by default it must go to high frequencies and in the case of $La_{2-x}Sr_xCuO_4$ (La214) the spectral weight has been shown to transfer to the 1 eV region [30]. A number of mechanisms have been proposed that would result in an incoherent conductivity spectrum [31–38]. The *c*-axis conductivity depression in both Y123 and Y124 occurs at a temperature scale that matches the spin susceptibility determined from the NMR measurements. This is shown in the inset of figure 2 where the Knight shift [39] is shown along with the experimental *c*-axis conductivity. The onset energy of the *c*-axis gap in YBCO is $\approx$200 cm^{-1} and the half-value point is at $\approx$300 cm^{-1}. Above 500 cm^{-1}, the *c*-axis conductivity is both temperature and frequency independent [29].

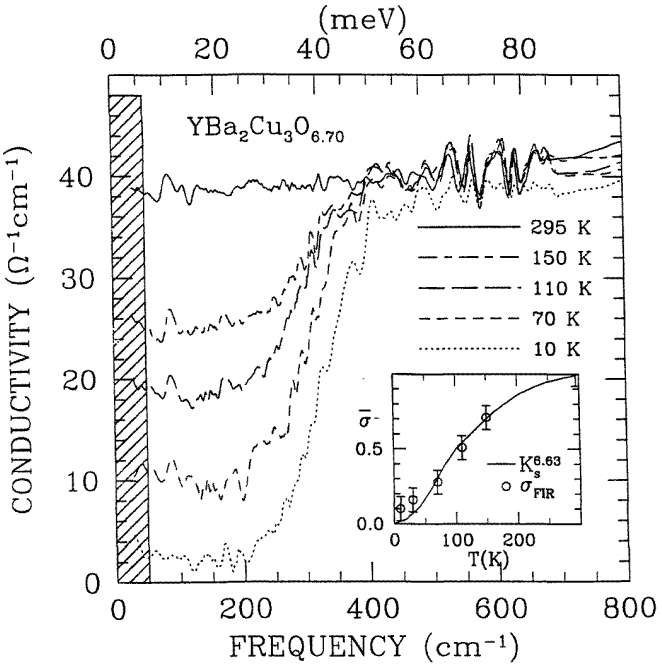

Figure 2. The *c*-axis conductivity of an underdoped Y123 crystal. The *c*-axis conductivity is temperature and frequency independent for $T > T^*$ but develops a marked gap-like depression below T^*. As the temperature is lowered the pseudogap deepens. Inset: the NMR Knight shift (normalized at 300 K) is plotted as a function of temperature for an underdoped Y123 crystal. The circles show the low-frequency *c*-axis conductivity for samples of the same doping level. The curves suggest that the Knight shift, a conventional measure of the density of states at the Fermi level, and the *c*-axis conductivity are depressed by the same process in the pseudogap state.

A pseudogap has also been observed in the *c*-axis conductivity of La214 where for $x = 0.14$ a very large gap has been reported [30] and for $x = 0.12$ a gap of the same magnitude as in YBCO can clearly be seen [40]. The $Pb_2Sr_2(Y/Ca)Cu_2O_8$ material also shows a *c*-axis pseudogap [41].

Recent angle-resolved photoemission (ARPES) results for $Bi_2Sr_2CaCu_2O_{8+\delta}$ (Bi2212) show evidence of a normal-state gap-like depression of the electronic density of states of underdoped cuprates as well [42–44]. The momentum dependence of this gap resembles that of the $d_{x^2-y^2}$ gap observed in the superconducting state [43]. This, and the fact that no significant changes are observed upon crossing into the superconducting regime, have led to the suggestion that the normal-state gap may be a precursor of the superconducting gap. As the doping level is increased to near- and above optimal the normal-state gap-like feature disappears.

In the following, we summarize the recent experimental optical results obtained from several series of HTSC materials at doping levels ranging from underdoped to strongly overdoped. We find that in the pseudogap state the optical response of underdoped cuprates is marked by an increase in coherence of the electronic system. Since the coherence effects are seen more clearly through the frequency-dependent charge-carrier scattering or memory function analysis, we have chosen to use this approach. The essential features of this very

general formalism are described in section 3. We will also restrict our survey to the *ab*-plane optical properties. The *c*-axis optical data are less complete since the large, thick crystals needed for this work are not available for all systems. We will, however, try to address the question of the correlation between the *ab*-plane and the *c*-axis pseudogap properties as we change materials, doping and temperature.

2. The experimental technique

In order to cover a broad range of doping regimes we performed reflectivity measurements upon three families of high-T_c cuprates: YBCO (including Y123 and Y124), Bi2212 and $Tl_2Sr_2CuO_{6+\delta}$ (Tl2201). This was necessary because, with the exception of La214, none of the existing cuprates allows one to explore a full spectrum of doping regimes. For instance, Y123 materials can be conveniently underdoped by reducing the amount of oxygen from the optimally doped level at $x = 6.95$. However, these crystals are not suitable for strong overdoping. On the contrary, Tl2201 samples could be only overdoped by introducing interstitial O atoms between the TlO planes so that T_c is suppressed from about 90 K in the *stoichiometric* composition down to less than 4 K in the overdoped composition. Single crystals of Bi2212 can be both overdoped and underdoped, but the suppression of the critical temperature is very limited on the overdoped side. We have also used Bi2212 crystals with 20% of Bi substituted for with Pb which allows one to achieve a higher degree of overdoping. The influence of disorder on the infrared response of YBCO crystals was studied by substituting Zn for the Cu atoms in the CuO_2 planes [45].

The response of YBCO crystals was studied in three carrier-density regimes: in an optimally doped Y123 crystal with the oxygen content set at $x = 6.95$ ($T_c = 93.5$ K), in the *same* crystal deoxygenated down to $x = 6.6$ ($T_c = 59$ K) [46] and in a double-chained Y124 crystal with $T_c = 82$ K [47]. The carrier density in the stoichiometric and naturally untwinned Y124 corresponds to that of Y123 samples with $x \simeq 6.85$. The Y123 crystal was mechanically detwinned so that both *a*- and *b*-axis components of the conductivity tensor were obtained independently, allowing us to probe the response of the CuO_2 planes *only* without any contribution from the charge reservoir structural blocks.

We have also performed reflectivity measurements on two underdoped ($T_c = 67$ K and $T_c = 82$ K), one optimally doped ($T_c = 90$ K), and one overdoped ($T_c = 82$ K) Bi2212 single crystal. All of the Bi2212 crystals were prepared from the as-grown crystals by annealing in argon and/or oxygen [48]. To achieve a higher degree of overdoping we have performed measurements on Pb-doped Bi2212, $Bi_{1.66}Pb_{0.34}Sr_2CaCu_2O_{8+\delta}$ ((Bi/Pb)2212), with $T_c = 70$ K (optimum $T_c = 88$ K). The two T2201 single crystals used in the measurements had T_cs of 90 K (the highest T_c achievable) and 23 K (strongly overdoped). The superconducting transition temperatures for all of the samples were measured in a SQUID magnetometer.

The reflectivity was measured over a broad energy range: from 30–50 cm^{-1} up to 20 000 cm^{-1} for Y123, Y124, and Bi2212 samples; from 30–50 cm^{-1} up to 50 000 cm^{-1} for Tl2201 samples. The far-infrared reflectance measurements were carried out using a rapid-scan interferometer with focused optics on a sample mounted in a continuous-flow cryostat. For near-infrared and visible measurements, a grating spectrometer with appropriate detector–filter combinations with overlapping frequency ranges was used. To obtain the absolute value of the reflectance, geometrical scattering losses were accounted for by *in situ* evaporation of a metallic film (Au or Al) onto the surface of the sample. The coated sample was then remeasured and the absolute value of the reflectance R is then given by the ratio of spectra before and after plating, corrected for the absolute reflectance

of the metallic film [49].

The complex optical conductivity $\sigma_1(\omega) + \mathrm{i}\sigma_2(\omega)$ of single-crystalline samples was obtained from Kramers–Kronig analysis of the reflectivity. To perform the required integrations it was necessary to extend the reflectance beyond the actually measured range [50]. Below the lowest frequency measured we have tried different types of reflectivity approximation, from the Hagen–Rubens formula to a straight line between unity at zero frequency and the last experimental point. We found that in the frequency region that will be of interest in this work ($\omega > 100$ cm^{-1}) the particular choice of low-frequency approximation is not important. At high frequencies, the reflectivity of Y123 and Y124 samples was extended using the results of previous measurements [51] up to 300 000 cm^{-1}. The reflectivity of Tl2201 was approximated by a constant between 50 000 and 200 000 cm^{-1}. For Bi2212, the results of ellipsometric measurements [52] were used between 20 000 and 50 000 cm^{-1} while above this frequency range a constant-reflectivity approximation was used up to 200 000 cm^{-1}. Above 200 000 cm^{-1} for Bi2212 and Tl2201 and above 300 000 cm^{-1} for YBCO the reflectivity was allowed to fall as ω^{-4}. In the case of the Y123 material we compared the optical constants obtained using Kramers–Kronig analysis with those obtained more directly by optical ellipsometry in the 2–5 eV range [53], and excellent agreement was found. This attests to the reliability of the results obtained through Kramers–Kronig analysis of the reflectance.

3. The extended drude formalism

3.1. The complex memory function

The classical Drude formula for the dynamical conductivity $\sigma(\omega) = \sigma_1(\omega) + \mathrm{i}\sigma_2(\omega)$ [50, 54] can be obtained by using a standard Boltzmann equation and approximating the collision integral with a single collision frequency $1/\tau$. The Drude formula describes the free-carrier contribution to $\sigma_1(\omega)$ as a Lorentzian peak centred at zero frequency with an oscillator strength of $\omega_p^2/8$, where $\omega_p^2 = [e^2/(3\pi^2\hbar)]\int \boldsymbol{v}\cdot\mathrm{d}\boldsymbol{S}_F$ and $\boldsymbol{v}$ is the electron velocity and $\boldsymbol{S}_F$ is the element of Fermi surface. For a spherical Fermi surface $\omega_p^2 = 4\pi n e^2/m_e$, where n is the free-carrier density and m_e is the electronic band mass. The Lorentzian width is determined by a constant scattering rate $1/\tau$. The imaginary part of $\sigma(\omega)$ is just the real part multiplied by $\omega\tau$:

$$\sigma(\omega) = \frac{1}{4\pi}\frac{\omega_p^2}{1/\tau - \mathrm{i}\omega} = \frac{\omega_p^2}{4\pi}\left[\frac{\tau}{1+(\omega\tau)^2} + \mathrm{i}\frac{\tau^2\omega}{1+(\omega\tau)^2}\right]. \tag{1}$$

A derivation of equation (1) by using the standard kinetic Boltzmann equation assumes that the elementary system excitations are well defined. However, a description of a system by using elementary excitations is possible, strictly speaking, only if the (energy) width of the wave packet representing the electronic excitation is small compared to the energy of the packet. In more formal language, for the approximations leading to equation (1) to be valid, a spectral function of electronic excitations defined as

$$A(\boldsymbol{k},\omega) = -\frac{1}{\pi}|\mathrm{Im}\,G(\boldsymbol{k},\omega)| = \frac{1}{\pi}\frac{\mathrm{Im}\,\Sigma(\omega)}{(\omega - \epsilon_k - \mathrm{Re}\,\Sigma(\omega))^2 + (\mathrm{Im}\,\Sigma(\omega))^2} \tag{2}$$

must be a narrow peak centred at $\omega = \epsilon_k + \mathrm{Re}\,\Sigma(\omega)$. Here $G(\boldsymbol{k},\omega)$ is a Green function of electronic excitation and $\Sigma(\omega)$ is the self-energy part. The narrowness of the peak means that the excitation energy must be much larger than the damping term $\gamma(\omega) = -2\,\mathrm{Im}\,\Sigma(\omega)$. This is certainly true in the case of standard Fermi-liquid theory, where $\mathrm{Re}\,\Sigma(\omega) \sim \omega$

and $\mathrm{Im}\,\Sigma(\omega) \sim \omega^2$ and thus the electronic excitations (quasiparticles) are well defined at zero temperature and energies close to the Fermi energy E_F [55]. It can also be shown [56] that a weak electron–phonon coupling, although it violates the quasiparticle description at energies very close to E_F, does not drastically change the transport properties at low temperatures, since in this case the number of electronic states where the quasiparticle description is violated is small. Therefore, the Drude formula is applicable only for simple metals at low frequencies and low temperatures where elastic scattering from impurities and weak quasielastic scattering from thermally excited excitations such as phonons dominate [50, 56].

On the other hand, following the original ideas of Anderson [57], it is now widely accepted that the electronic system of HTSC materials represents a new kind of quantum liquid and the simple Fermi-liquid quasiparticle description is not applicable to the normal-state properties of these materials. For example, the key ingredient of the phenomenological 'marginal' Fermi-liquid theory [58], advanced to explain these properties, is the assumption that the $\mathrm{Im}\,\Sigma(\omega) \sim \omega$ and, consequently, $\mathrm{Re}\,\Sigma(\omega)$ diverges logarithmically at the Fermi energy, thus making $G(\boldsymbol{k}, \omega)$ entirely incoherent at E_F. On a more microscopic level, a similar result is expected for the quasi-one-dimensional Hubbard model, which was identified by Anderson as an appropriate paradigm for the resonant-valence-bond (RVB) description [57]. Even in more Fermi-liquid-like scenarios, sufficiently strong coupling of an electronic system to a bosonic energy spectrum may result in a violation of the quasiparticle description [56]. In addition, the Fermi energy is estimated to be only $E_F = 1$–2 eV, which is not much larger than the energies probed in infrared experiments (4–300 meV). Such a low E_F may be another reason for violation of a quasiparticle description. Since this implies the absence of well-defined elementary excitations, the approximations used to obtain equation (1) are not justified. The breakdown of the quasiparticle description has also been discussed by Emery and Kivelson in the context of abnormally short values of the mean free path that lead to the violation of the Ioffe–Regel criterion [59].

However, the optical conductivity can be described in a much more general way by making the damping term in the Drude formula complex and frequency dependent: $1/\tau = M(\omega) = M'(\omega) + \mathrm{i}M''(\omega)$, where $M(\omega)$ is called a memory function [60–62]. $M(\omega)$ satisfies $M'(\omega) = M'(-\omega)$ and $M''(\omega) = -M''(-\omega)$. The consequences of this formalism, usually referred to as the extended Drude model, have been derived for the infrared conductivity of metals with a strong electron–phonon interaction by Allen [63] and Allen and Mikkelsen [60] for the case of zero temperature. The analysis was later extended for the case of finite temperatures by Shulga *et al* [56]. It is also believed that the resulting theory is valid in the case of the coupling of a Fermi liquid to any bosonic energy spectrum. Some aspects of the extended Drude model were also examined in detail by Götze and Wölfe [62]. We are not aware of any quantitative predictions regarding the extended Drude model in the completely non-Fermi-liquid scenario, such as the Luttinger-liquid theory. Therefore, in the following we will employ the Fermi-liquid terminology. The formalism has been previously applied to transition metal compounds [60], heavy-fermion materials [64, 65], and the HTSC cuprates [15, 66–69].

Rewriting the complex conductivity $\sigma(\omega)$ in terms of a complex memory function, $M(\omega, T) = 1/\tau(\omega, T) - \mathrm{i}\omega\lambda(\omega, T)$, one obtains [50, 61]

$$\sigma(\omega, T) = \frac{1}{4\pi}\frac{\omega_p^2}{M(\omega, T) - \mathrm{i}\omega} = \frac{1}{4\pi}\frac{\omega_p^2}{1/\tau(\omega, T) - \mathrm{i}\omega[1 + \lambda(\omega, T)]}. \tag{3}$$

Although, in the case of a metal, equation (3) can be obtained using the Boltzmann-equation formalism with a frequency-dependent scattering rate [60], this form has in fact a

range of validity more general than the Boltzmann-equation approach [60, 61]. Adopting the Boltzmann-type terminology, the quantities $1/\tau(\omega, T)$ and $\lambda(\omega, T)$ describe the frequency-dependent scattering rate and mass enhancement of electronic excitations due to many-body interactions.

Using the more general form of equation (3), one can check the range of validity of the classical Drude formula of equation (1) by expanding the memory function into Taylor series for small frequencies:

$$\lim_{\omega\to 0} M(\omega) = \frac{1}{\tau(0)} - \mathrm{i}\lambda(0)\omega + \mathrm{O}(\omega^2). \tag{4}$$

Substituting this into equation (3) one finds

$$\sigma(\omega, T) = \frac{1}{4\pi}\frac{\omega_p^2}{1/\tau(0) - \mathrm{i}\omega(1+\lambda(0))} \tag{5}$$

recovering equation (1). The classical Drude result is thus valid whenever expansion of equation (4) makes sense and $\lambda(0)$ is small compared to unity.

Equation (3) can be reduced to the familiar Drude form of equation (1) by introducing the so-called renormalized scattering rate $1/\tau^*(\omega, T) = 1/[\tau(\omega, T)(1+\lambda(\omega, T))]$ and the effective plasma frequency $\omega_p^{*2}(\omega, T) = \omega_p^2/(1+\lambda(\omega, T))$:

$$\sigma(\omega, T) = \frac{1}{4\pi}\frac{\omega_p^{*2}(\omega, T)}{1/\tau^*(\omega, T) - \mathrm{i}\omega}. \tag{6}$$

As can be seen from this equation, the optical conductivity is now composed of an infinite set of Drude peaks, each describing $\sigma(\omega)$ in the vicinity of a particular frequency ω with a set of parameters $1/\tau^*(\omega)$ and $\lambda(\omega)$ (for simplicity in the following we will drop the temperature parameter when it is not relevant to a discussion). $1/\tau^*(\omega)$ has the phenomenological meaning of a width of the Drude peak local to a frequency ω while $\lambda(\omega)$ represents the interaction-induced velocity renormalization. The renormalized scattering rate $1/\tau^*(\omega)$ is not causal and, other than the local Drude width, does not have a real physical sense as it includes both the velocity renormalization and the lifetime effects.

On the other hand, $1/\tau(\omega)$ is, up to a constant, the real part of $1/\sigma(\omega)$:

$$1/\tau(\omega) = \frac{\omega_p^2}{4\pi}\mathrm{Re}\left(\frac{1}{\sigma(\omega)}\right) \tag{7}$$

that is, a real part of a physical response function. In the limit of zero frequency the normal-state optical conductivity is completely real and equation (4) becomes $1/\sigma_{dc}(T) = \rho_{dc}(T) = m_e/(\tau(T)ne^2)$, where $\rho_{dc}(T)$ is the dc resistivity. This is the same form as the relaxation-time expression for the dc resistivity of a free-electron gas and therefore $\tau(\omega, T)|_{\omega=0}$ may be viewed as an electronic lifetime.

The mass enhancement factor $\lambda(\omega)$ is given as the imaginary part of $1/\sigma(\omega)$:

$$1 + \lambda(\omega) = -\frac{\omega_p^2}{4\pi}\frac{1}{\omega}\mathrm{Im}\left(\frac{1}{\sigma(\omega)}\right). \tag{8}$$

The total plasma frequency ω_p^2 in equations (7), (8) can be can be found from the sum rule $\int_0^\infty \sigma_1(\omega)\,\mathrm{d}\omega = \omega_p^2/8$. Since $\sigma(\omega)$ is causal, $\lambda(\omega)$ and $1/\tau(\omega)$ are not independent and are related by the Kramers–Kronig relation [50]. Using the relations $1/\tau(\omega) = 1/\tau(-\omega)$ and $\lambda(\omega) = \lambda(-\omega)$ we obtain

$$\lambda(\omega) = \frac{2}{\pi}\mathcal{P}\int_0^\infty \frac{1/\tau(\Omega)}{\Omega^2 - \omega^2}\,\mathrm{d}\Omega \tag{9}$$

$$1/\tau(\infty) - 1/\tau(\omega) = \frac{2}{\pi}\mathcal{P}\int_0^\infty \frac{\Omega^2\lambda(\Omega)}{\Omega^2 - \omega^2}\,\mathrm{d}\Omega. \tag{10}$$

If $1/\tau(\omega)$ and $\lambda(\omega)$ have no poles at $\omega = 0$ one immediately obtains the following useful relation:

$$1/\tau(\infty) - 1/\tau(0) = \frac{2}{\pi}\int_0^\infty \lambda(\Omega)\,\mathrm{d}\Omega. \tag{11}$$

We see that the complex memory function $M(\omega)$ is a physical response function and experimental data can be presented in terms of $M(\omega, T)$ or the complex optical conductivity $\sigma(\omega, T)$ equally well. The particular choice should be made judging from the situation at hand. For example, the memory function analysis may be useful if one is interested in the relaxation processes that determine a system response to electromagnetic radiation. Also, in certain cases the memory function is easier to calculate analytically, thus making it easier to analyse the physics behind the system behaviour using experimental results for $M(\omega)$. For example, simple analytical formulae for $M(\omega)$ have been derived for electron–phonon scattering while the optical conductivity has to be calculated numerically [56].

Finally, we would like to stress that, although equation (3) is very general, obviously the *interpretation* of experimental results for $M(\omega, T)$ in terms of scattering rate and mass enhancement only makes sense when a (generalized) Boltzmann equation can be used. For example, if the optical response is determined by two distinct charge-carrier systems (two-component) so that the optical conductivity takes the form

$$\sigma(\omega) = \sigma^I(\omega) + \sigma^{II}(\omega) \tag{12}$$

the interpretation of $M'(\omega)$ and $M''(\omega)$ as a scattering rate and a mass enhancement is meaningless, as can be seen from equations (7), (8). This is the case if an interband transition is present in the same frequency region where there is an intraband response. We note, however, that the form (12) can arise from a double-relaxation process (two different scattering mechanisms) as well [60].

Since in the superconducting state $\sigma_1(\omega)$ is suppressed, the low-frequency optical conductivity is dominated by the imaginary term $\sigma_2(\omega) = \omega_{ps}^2/(4\pi\omega)$. In this case the low-frequency mass-enhancement factor gives a ratio of the total plasma frequency, ω_p^2, to the plasma frequency of the superconducting carriers, ω_{ps}^2: $1 + \lambda(\omega) = \omega_p^2/\omega_{ps}^2$.

3.2. Electron–boson scattering

Memory function analysis has been most extensively developed for the case of electron–phonon scattering [60, 63, 56]. It can be shown in the limit of frequencies comparable to the Debye frequency and/or high enough temperature that the quasiparticle description breaks down [56]. Using more general many-body calculations Shulga *et al* obtained the following expression for $1/\tau(\omega, T)$:

$$\frac{1}{\tau}(\omega, T) = \frac{\pi}{\omega}\int_0^\infty \mathrm{d}\Omega\ \alpha_{tr}^2(\Omega)F(\Omega)\left[2\omega\coth\left(\frac{\Omega}{2T}\right) - (\omega+\Omega)\coth\left(\frac{\omega+\Omega}{2T}\right) + (\omega-\Omega)\coth\left(\frac{\omega-\Omega}{2T}\right)\right] + \frac{1}{\tau_{imp}}. \tag{13}$$

Here $\alpha_{tr}^2(\Omega)F(\Omega)$ is a phonon density of states weighted by the amplitude for large-angle scattering on the Fermi surface and T is measured in frequency units. The last term in

(13) represents impurity scattering. In the limit of zero temperature this reduces to Allen's result [63]:

$$\frac{1}{\tau}(\omega) = \frac{2\pi}{\omega}\int_0^{\omega} \mathrm{d}\Omega\ (\omega - \Omega)\alpha_{tr}^2(\Omega)F(\Omega) + \frac{1}{\tau_{imp}}. \tag{14}$$

The dc scattering rate is obtained in the limit of $\omega = 0$ in equation (13):

$$\frac{1}{\tau}(0, T) = \pi\int_0^{\infty} \mathrm{d}\Omega\ \alpha_{tr}^2(\Omega)F(\Omega)\frac{\Omega}{T}\sinh^{-2}\left(\frac{\Omega}{2T}\right) + \frac{1}{\tau_{imp}}. \tag{15}$$

At temperatures much higher than the phonon spectrum upper-energy cut-off, $T \gg \Omega_c$, the above expression reduces to

$$\lim_{T/\Omega_c\to\infty}\frac{1}{\tau}(0, T) = 4\pi T\int_0^{\infty} \mathrm{d}\Omega\ \frac{\alpha_{tr}^2(\Omega)F(\Omega)}{\Omega} + \frac{1}{\tau_{imp}} \tag{16}$$

which is just the familiar result that the high-temperature electron–phonon contribution to a dc resistivity is linear in temperature.

In the limit of high ω, $\omega \gg \Omega_c$,

$$\lim_{\omega/\Omega_c\to\infty}\frac{1}{\tau}(\omega, T) = 2\pi\int_0^{\infty} \mathrm{d}\Omega\ \alpha_{tr}^2(\Omega)F(\Omega)\coth\left(\frac{\Omega}{2T}\right) + \frac{1}{\tau_{imp}} \tag{17}$$

which at high temperatures, $T \gg \Omega_c$, assumes the same value as the zero-frequency limit (16). Therefore, at very high temperatures the scattering rate becomes frequency independent and equation (6) reduces to the classical Drude expression (1).

We note that the effective scattering rate $1/\tau(\omega)$ is different from the quasiparticle attenuation $\gamma(\omega)$. For example, at zero temperature $\gamma(\omega)$ is given by [63, 70]

$$\gamma(\omega) = -2\,\mathrm{Im}\,\Sigma(\omega) = 2\pi\int_0^{\omega} \mathrm{d}\Omega\ \alpha^2(\Omega)F(\Omega) + \frac{1}{\tau_{imp}}. \tag{18}$$

Here $\alpha^2(\Omega)F(\Omega)$ is the isotropically weighted phonon density of states. One can see from equations (14), (18) that at $T = 0$ the effective scattering rate $1/\tau(\omega)$ is, if the difference between α_{tr}^2 and α^2 is neglected, an *average* of $\gamma(\omega)$ over frequencies from 0 to ω and therefore $\gamma(\omega)$ enters into the effective scattering rate in a way non-local in frequency [56, 61, 63]. As a consequence, $1/\tau(\omega)$ is actually equal to the quasiparticle attenuation $\gamma(\omega)$ only at $\omega = 0$, where $1/\tau(0) = \gamma(0) = 1/\tau_{imp}$. The two quantities also asymptotically approach each other in the limit of high frequencies, $\omega \gg \Omega_c$, where both $\gamma(\omega)$ and $1/\tau(\omega)$ become frequency independent. As the temperature is increased, the difference between $\gamma(\omega)$ and $1/\tau(\omega)$ is smeared out, and in the limit of $T \gg \Omega_c$ they are asymptotically equal. Generally, however, $\tau(\omega, T)$ deviates from the quasiparticle lifetime $\gamma^{-1}(\omega, T)$.

Equations (13), (14), which have been derived for electron–phonon scattering, are believed to be valid in the case of the coupling of an electronic spectrum to any bosonic excitations [64, 65]. In this case the Eliashberg function $\alpha_{tr}^2(\Omega)F(\Omega)$ in equations (13), (14) is replaced by the corresponding, suitably weighted, bosonic spectral density $\mathcal{A}_{tr}(\omega)$. To give a flavour of the results expected on the basis of equations (13), (14) we will perform calculations for several model shapes of $\mathcal{A}_{tr}(\omega)$: a δ-peak, a 'square'-like spectrum and $\mathcal{A}_{tr}(\omega) = \Gamma\omega/(\Gamma^2 + \omega^2)$. The last spectrum is believed to be appropriate for scattering of electrons on spin fluctuations [71].

In the case of $\mathcal{A}_{tr}(\omega) = \omega_0\delta(\omega - \omega_0)$ the integration of equation (13) can easily be performed. The effective-mass enhancement $\lambda(\omega)$ can be calculated using the Kramers–Kronig relation (9). As soon as both $1/\tau(\omega, T)$ and $\lambda(\omega, T)$ are known, the optical conductivity can be calculated using equation (3). The impurity scattering has been set

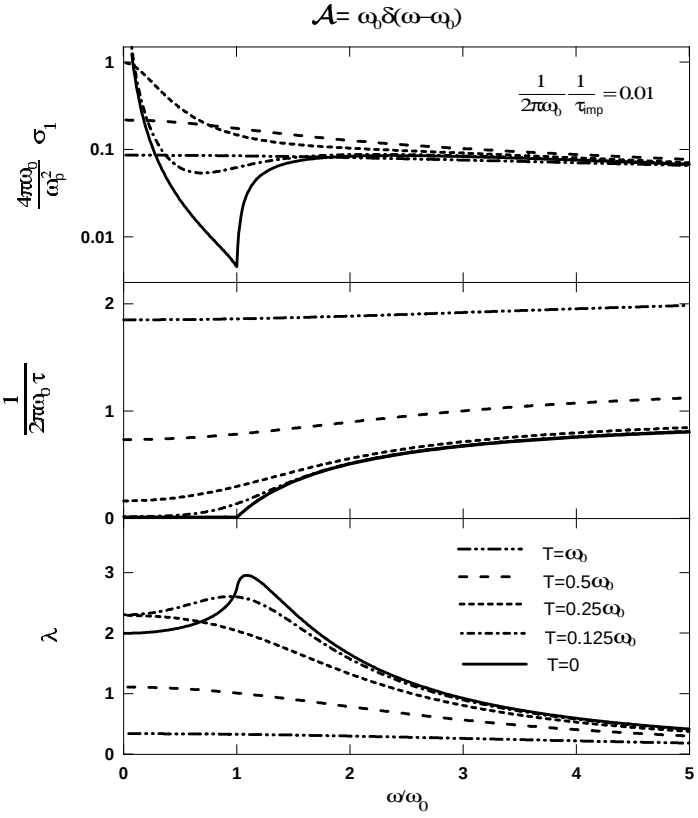

Figure 3. Electron–boson model calculations with the boson spectral density $\mathcal{A}_{tr}(\Omega) = \omega_0\delta(\omega-\omega_0)$. The top panel shows the optical conductivity, the middle panel shows the scattering rate and the bottom panel shows the mass renormalization. The coupling constant is equal to 1.

to $1/(2\pi\omega_0\tau_{imp}) = 0.01$. The results obtained are presented in figure 3 at five different temperatures: $T = 0, 0.125\omega_0, 0.25\omega_0, 0.5\omega_0, \omega_0$.

For the two other choices of $\mathcal{A}_{tr}(\omega)$, the integration of equation (13) was performed numerically. We then used the Kramers–Kronig relation to obtain $\lambda(\omega, T)$. The same impurity scattering rate as in the case of the δ-function was used to calculate $\sigma_1(\omega)$. The results are presented in figure 4 and figure 5 at different temperatures, measured in units of the characteristic frequency of the bosonic spectrum $\mathcal{A}_{tr}(\omega)$.

As was discussed above, if the $\mathcal{A}_{tr}(\omega)$ spectrum has a high-energy cut-off, $1/\tau(\omega, T)$ saturates at frequencies that are much higher than the cut-off. The value of $1/\tau(\omega, T)$ in the saturation regime is strongly temperature dependent, and linear in T at high enough temperatures according to (17). However, if there is no cut-off in $\mathcal{A}_{tr}(\omega)$, as in the case of the magnetic spectrum in figure 5, there is no high-frequency saturation of $1/\tau(\omega, T)$—rather it continues to increase. The temperature dependence of the absolute value of the scattering rate is, however, still strong.

In figure 3, the effective-mass enhancement $\lambda(\omega, T)$ is larger at low frequencies and decreases to zero at high frequencies. This has a simple physical interpretation that at high frequencies the boson 'cloud' is not capable of following the charge carriers. The

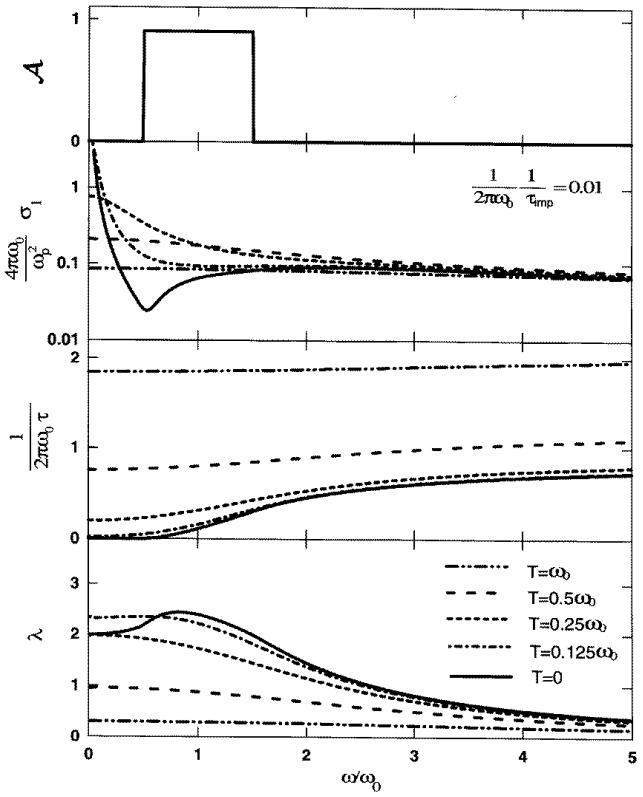

Figure 4. Electron–boson model calculations. The top panel shows the bosonic spectral density, here a 'square' spectrum, the next shows the optical conductivity, the next shows the scattering rate and the bottom panel shows the mass renormalization. The coupling constant is equal to 1.

sharp increase in the low-temperature λ around the frequency of the bosonic excitation ω_0 corresponds to the onset of a boson-emission process, since only carriers with energy greater than $\hbar\omega_0$ can emit a boson. A similar onset can be seen in figure 4. In the case of the magnetic $\mathcal{A}_{tr}(\omega)$, this feature is not observed since bosons can be emitted by a carrier with arbitrarily small energy. At high temperatures λ asymptotically approaches zero, in agreement with the frequency-independent scattering rate $1/\tau$.

The low-temperature conductivity in figure 3 shows a pronounced absorption band, called a Holstein band, with a sharp onset at ω_0. The band corresponds to an additional absorption channel associated with boson-emission processes. A similar absorption onset can be seen in figure 4 but not in figure 5. The reason for this, as in the case of λ, is the large boson spectral density at all non-zero frequencies for the magnetic $\mathcal{A}_{tr}(\omega)$. As the temperature is increased, all sharp features in σ_1 are smeared out and at very high temperatures the conductivity can be described by the single Lorentzian of equation (1).

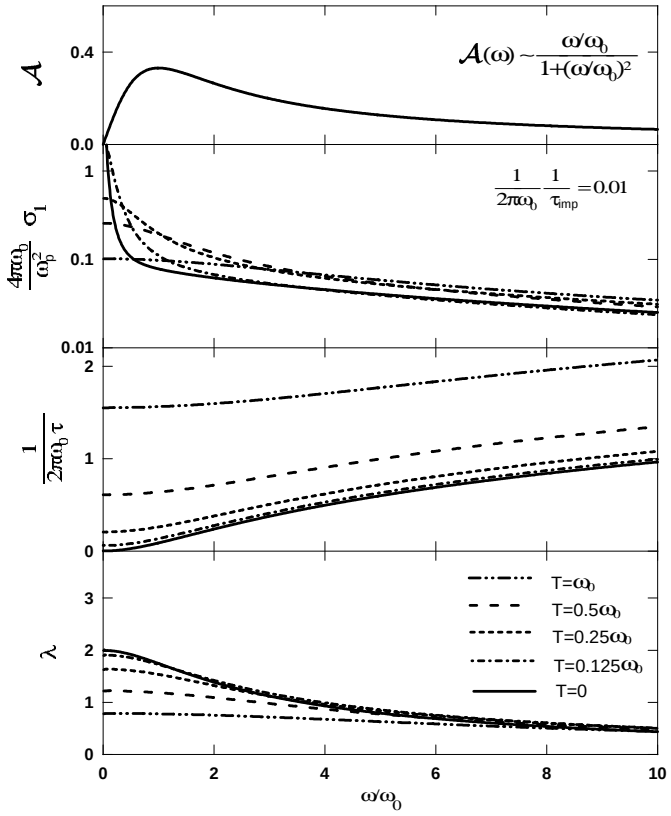

Figure 5. Electron–boson model calculations. The top panel shows the bosonic spectral density, the next shows the optical conductivity, the next shows the scattering rate and the bottom panel shows the mass renormalization. The coupling constant is equal to 1.

4. Experimental results

This section is divided into three subsections: underdoped, optimally doped and overdoped cuprates. In each of the subsections we first present the raw experimental results in the form of absorption $A(\omega) = 1 - R(\omega)$ for a selected material at many different temperatures. Before we proceed to the memory function analysis, we will also present the results for the same material in terms of more commonly used real optical conductivity $\sigma_1(\omega)$. However, we will focus the analysis on the real and imaginary parts of the memory function $M(\omega) = M'(\omega) + \mathrm{i}M''(\omega)$, that will be presented for several materials on a second diagram in each subsection. While for a selected material in each subsection we will show many different temperatures, to simplify the diagrams for others, only three temperatures will be shown: $T = 300$ K, $T \simeq T_c$ and the lowest (superconducting) temperature.

We note here again that we are fully aware that in most real situations, and especially in HTSC, the real and imaginary parts of $M(\omega)$ are not solely determined by the scattering effects and the corresponding enhancement of an effective mass. Nevertheless, mostly for historical reasons, we will refer to the effective scattering rate and to the effective mass defined as $1/\tau(\omega) = M'(\omega)$ and $m^* = 1 + \lambda(\omega) = 1 - M''(\omega)/\omega$ respectively. Keeping this in mind, we will now present the experimental results and indicate the common trends,

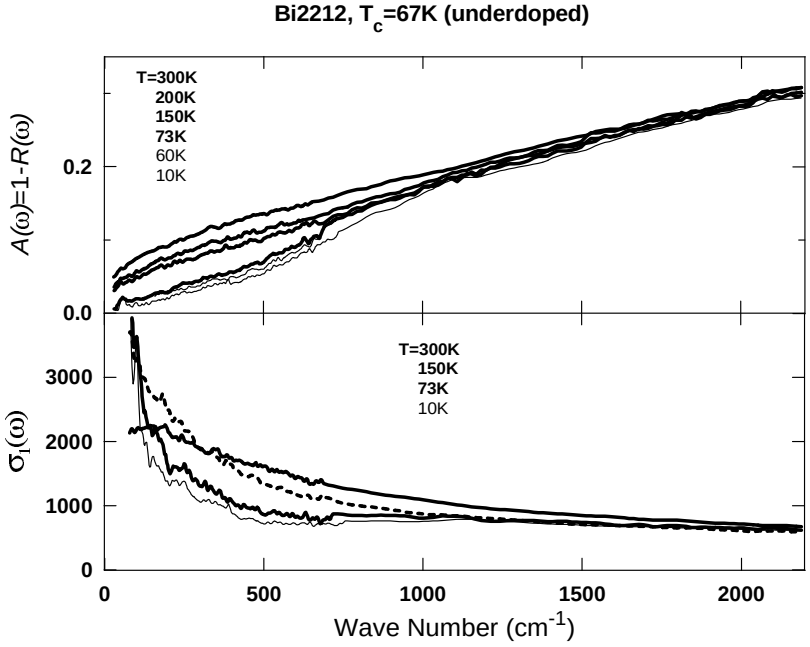

Figure 6. The absorption $A = 1 - R$, top panel, and the optical conductivity $\sigma_1(\omega)$ for underdoped Bi2212 ($T_c = 67$ K). The absorption rises linearly at high temperatures but develops a depression below 800 cm^{-1} due to the formation of the pseudogap. In the optical conductivity the pseudogap shows up as a narrowing of the coherent Drude peak at low frequency.

leaving the interpretation for the discussion section. Since we will mainly be interested in the evolution of the optical response in the pseudogap energy region we will present the experimental data up to 2000 cm^{-1} only.

4.1. Underdoped cuprates

A typical plot of the temperature dependence of the raw absorption data $A(\omega, T)$ for an underdoped HTSC is shown in figure 6, this particular example being underdoped Bi2212 material with $T_c = 67$ K. In the temperature range 300–150 K the absolute value of the low-frequency absorption decreases smoothly with decreasing temperature without any sharp features. However, at a temperature $T < T^* \simeq 150$ K, the absorption below 600–700 cm^{-1} starts to decrease faster than at higher frequencies, developing a threshold structure which is characteristic for an underdoped HTSC in the pseudogap state.

The corresponding changes in the real part of optical conductivity $\sigma_1(\omega)$ are also shown in figure 6 at selected temperatures. The in-plane response of all samples is metallic, i.e. the absolute value of $\sigma_1(\omega)$ decreases from the dc value with increasing ω. However, while the $\sigma_1(\omega)$ spectra are quite broad at temperatures above T^*, the rapid decrease of the low-frequency absorption below T^* results in an abrupt narrowing of the low-frequency conductivity with substantial spectral weight being transferred towards zero frequency. As temperature is reduced below T_c, no dramatic changes are observed in the optical response of underdoped cuprates: the only change is just a *continued* narrowing of the intense low-frequency peak, that has already been initiated in the normal state.

The scattering rate $1/\tau$ and the effective mass $m^*/m_e = 1 + \lambda$ for the Bi2212

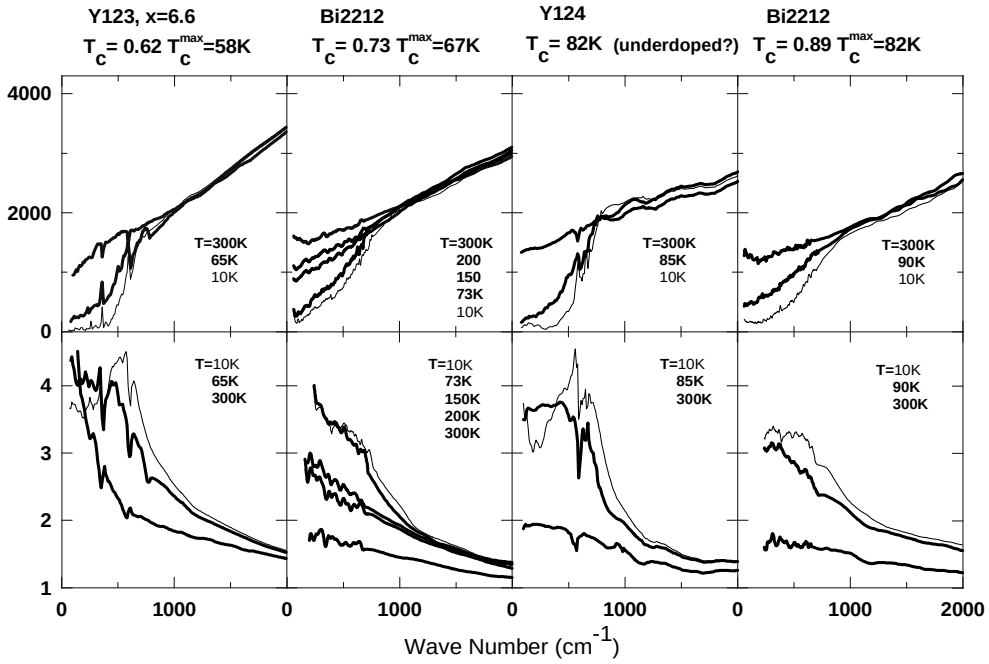

Figure 7. The frequency-dependent scattering rate, top row, and the mass renormalization for a series of underdoped cuprate superconductors, bottom row. The scattering rate curves are essentially temperature independent above 1000 cm^{-1} but develop a depression at low temperature and low frequencies. The effective mass is enhanced at low temperature and low frequencies.

crystal with $T_c = 67$ K, calculated from the optical conductivity using the formulae described in section 3, are shown in figure 7. We have used a plasma frequency value of $\omega_p = 14\,300$ cm^{-1}, obtained by using the conductivity sum-rule analysis [50, 72] with integration of $\sigma_1(\omega)$ over all frequencies up to 1 eV. We note that the value of ω_p obtained in this way is somewhat ambiguous since there is no clear separation between the frequency regions of the free- and bound-carrier optical responses. However, a particular choice of ω_p only multiplies $1/\tau(\omega)$ and $m^*(\omega)$ by a constant. Since in this paper we are mostly interested in the *frequency dependence* of these quantities, the exact value of ω_p is not of primary importance. To keep the absolute values consistent throughout the paper, in the Bi2212 and Tl2201 series we will use plasma frequency values obtained by integrating the real part of the optical conductivity up to 1 eV, which seems to be an energy below which the conductivity is substantially changed by doping [16, 72]. In the YBCO series we will use an energy of 1.5 eV as an upper integration limit since the reflectivity plasma minimum is higher for these materials [50].

The scattering rate $1/\tau(\omega)$ of underdoped Bi2212 with $T_c = 67$ K is linear at frequencies from 800 cm^{-1} to at least 3000 cm^{-1} at all temperatures. While at room temperature the low-frequency $1/\tau(\omega)$ deviates upwards from the high-frequency linear law, at $T = 200$ K the spectrum is linear over the whole frequency range from 100 to 3000 cm^{-1}. However, as temperature is reduced below T^*, the scattering rate is suppressed more rapidly at low

frequencies ($\omega < 700$ cm^{-1}) while it remains nearly unaffected at higher energies. A result of this development is the appearance of a distinct threshold in the $1/\tau(\omega)$ spectra. Another interesting phenomenon, that we will return to later, is the remarkable temperature independence of the high-frequency $1/\tau(\omega)$.

Like other quantities, the effective mass $m^*(\omega)$ displays a rapid change at frequencies below 700 cm^{-1} as temperature is reduced below T^*. We note that the narrowing of the low-frequency optical conductivity is a result of *both* a decrease of $1/\tau(\omega)$ and an increase of $m^*(\omega)$ since heavy carriers are more difficult to scatter. The width of a conductivity peak is determined by a renormalized scattering rate $1/\tau^*(\omega) = m_e/(\tau(\omega)m^*(\omega))$. At low temperatures the effective mass saturates at $m^*(0) \simeq 3$–4.

The experimental results obtained for several other cuprate materials at different doping levels in the underdoped state are qualitatively similar. In the rest of figure 7. we show the effective scattering rate and the carrier mass obtained for Y123 with oxygen content $x = 6.6$ and $T_c = 58$ K, naturally underdoped Y124 with $T_c = 80$ K, and slightly underdoped Bi2212 with $T_c = 82$ K. The in-plane plasma frequency ω_p, related to the conductivity by $\omega_p^2/8 = \int_0^\infty \sigma_1(\omega)\ \mathrm{d}\omega$, scales with T_c in accordance with earlier measurements [16, 72]. Integration of the conductivity up to 1.5 eV yields the following values of the plasma frequency: 15 000 cm^{-1} in $YBa_2Cu_3O_{6.6}$, 16 000 cm^{-1} in $YBa_2Cu_4O_8$ and 15 600 cm^{-1} in Bi2212. For clarity, only three temperatures are shown for each material: room temperature, just above T_c and well below T_c.

All of the samples show the same characteristic suppression of the amplitude of the scattering rate at $T < T^*$, which seems to increase as the doping level decreases. Despite the differences in the values of T^* in the different samples, the energy scale associated with the suppression of $1/\tau(\omega)$, does not change significantly with doping. In particular, a deviation from the linear behaviour in all of the samples studied occurs at the same frequency $\omega < 700$ cm^{-1}. As the doping level is increased towards the optimal, the normal-state depression of $1/\tau(\omega)$ becomes progressively shallower, while in the superconducting state the depression remains almost unchanged. The net effect is that the difference between the low-temperature normal-state and the superconducting-state $1/\tau(\omega)$ becomes more prominent as the doping level approaches the optimal. At the same time, qualitatively, the shape of the normal-state $1/\tau(\omega)$ at $T < T^*$ remains similar to that in the superconducting state. With the exception of the Y124 sample, for all of the samples the high-frequency $1/\tau(\omega)$ is linear up to at least 3000 cm^{-1} (2000 cm^{-1} for Y124) and it is nearly temperature independent. The low-temperature effective mass $m^*(\omega)$ becomes enhanced at low frequencies when temperature is reduced below T^*. In all of the samples $m^*(\omega)$ saturates at about the same value of $\approx$3–4.

To summarize, the optical response of underdoped cuprates is characterized by the following generic features. (i) The scattering rate is nearly linear with ω at $T > T^*$. (ii) At $T < T^*$ (the pseudogap state) the low-frequency scattering rate is suppressed corresponding to the rapid narrowing of the Drude-like feature in the conductivity spectra. The energy scale associated with the changes of $1/\tau(\omega)$ spectra was found to be the same in all of the samples. The magnitude of the depression weakens as the doping is increased towards the optimal level. (iii) The high-frequency $1/\tau(\omega)$ remains effectively temperature independent and linear from 700 cm^{-1} up to at least 3000 cm^{-1} in most underdoped HTSC samples.

4.2. Optimally doped and lightly overdoped cuprates

A similar threshold structure in the raw absorption spectra is observed for the optimally doped crystals as well. As an example, in figure 8 we show absorption and conductivity

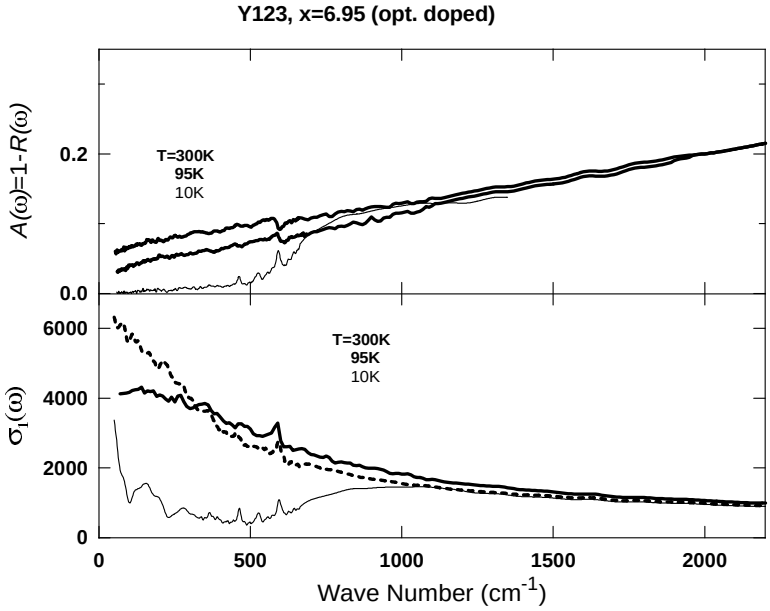

Figure 8. The absorption $A = 1 - R$ and the optical conductivity for optimally doped Y123 with $x = 6.95$ ($T_c = 93.5$ K). A depression of A is seen below 800 cm^{-1} but only below the superconducting transition temperature T_c. The same is true for the characteristic narrowing of the optical conductivity.

data obtained from optimally doped Y123 material. The important difference from the underdoped cuprates is that now a threshold in $A(\omega)$ develops only at temperatures below T_c. The corresponding $1/\tau(\omega)$ and $m^*(\omega)$ spectra are plotted in figure 9. We have used a plasma frequency $\omega_p = 18\,000$ cm^{-1}, obtained from the sum-rule analysis with integration up to 1.5 eV. All of the optical constants show the same characteristic features as in underdoped cuprates but the onset temperature is determined now by T_c. A remarkable feature of the optimally doped samples is the similarity between the behaviour of the superconducting-state optical response obtained in these crystals and the data obtained for the underdoped materials at $T_c < T < T^*$. This would be consistent with the notion that the T_c- and T^*-boundaries in figure 1 cross at around the optimal doping level. As a result, the difference between the normal-state and the superconducting-state spectra becomes dramatic in optimally doped samples.

In the normal state, as the temperature is reduced from 300 K down to $T \simeq T_c$, both the scattering rate and the renormalized effective mass, in optimally doped samples, show relatively minor changes. These changes are mainly restricted to the decrease of the absolute value of $1/\tau(\omega)$ in the low-frequency parts of the spectra. However, in contrast to what occurs for the underdoped materials, the normal-state scattering rate in Y123 does not reveal any sharp changes in the frequency dependence as the temperature is reduced.

In the rest of figure 9 we show data obtained on Bi2212 with $T_c = 90$ K and Tl2201 with $T_c = 90$ K. We should note that although we assigned the material Tl2201 to this section, the peak in T_c as a function of doping has not observed for Tl2201 and some data suggest that this material may be somewhat overdoped [72]. The plasma frequency used for Bi2212 was $\omega_p = 16\,000$ cm^{-1} and for Tl2201 $\omega_p = 15\,300$ cm^{-1}. The normal-state spectra of $1/\tau(\omega)$ are featureless. In the case of Tl2201 the threshold structure appears

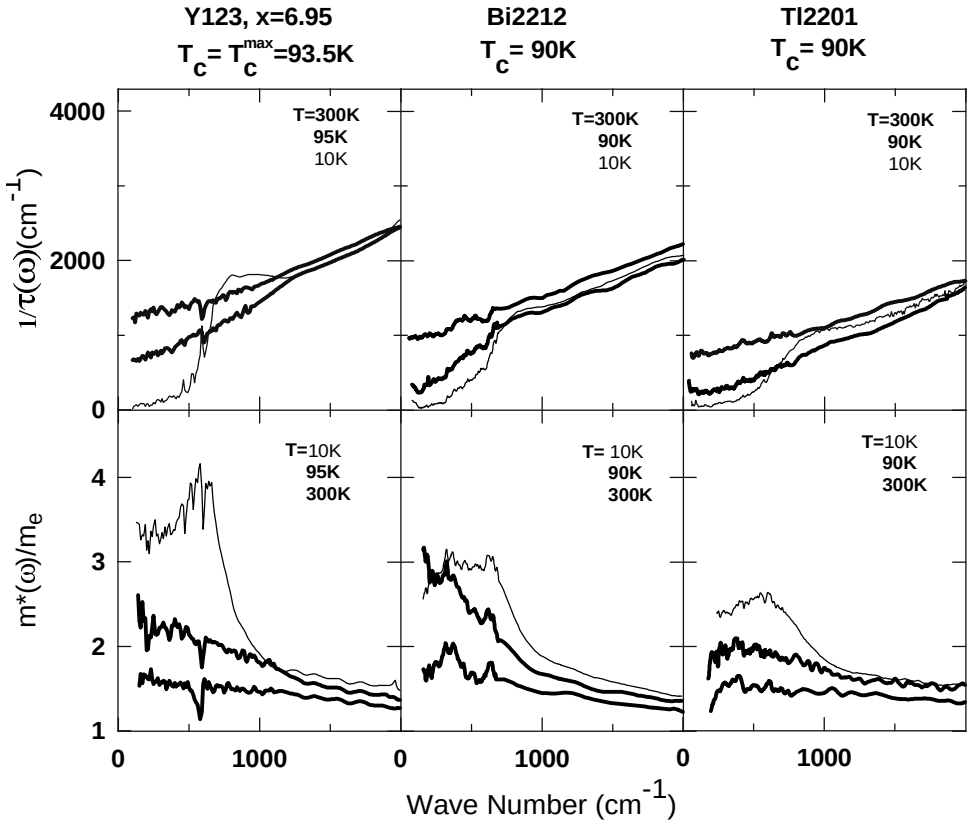

Figure 9. The scattering rate and the effective mass for samples close to optimal doping. The scattering rate now has a degree of temperature dependence at low frequencies. In the superconducting state the scattering rate is depressed at low frequencies.

only at $T < T_c$ but in Bi2212 a weak structure can still be seen at $T = 90$ K. In fact, it persists even in the lightly overdoped samples. Thus it is possible that the pseudogap state in figure 1 can penetrate somewhat into the overdoped regime. Qualitatively, the depression in $1/\tau(\omega)$ at $T < T_c$ in the optimally doped cuprates is very similar to what is observed in the $1/\tau(\omega)$ spectra in the pseudogap state of the underdoped cuprates. However, in contrast with the case for the underdoped materials, the temperature dependence of the scattering rate now seems to extend over a broader frequency range. In particular, in the Bi2212 and Tl2201 samples the $1/\tau(\omega)$ spectra reveal some shift in the high-frequency part (above the 700 cm^{-1} threshold) whereas in the underdoped materials no temperature dependence was observed at these frequencies.

Another weak feature that seems to be common for both the optimally doped Y123 and $T_c = 90$ K Tl2201 is an 'overshoot' of the superconducting-state $1/\tau(\omega)$ above the spectrum of $1/\tau(\omega)$ for $T \simeq T_c$.

In summary, the response of the optimally doped high-T_c cuprates demonstrates the following features: (i) a threshold feature in the $1/\tau(\omega)$ spectra at $T > T_c$ is either strongly suppressed or disappears completely when the doping level approaches optimal; (ii) the high-frequency $1/\tau(\omega)$ remains linear but may acquire a weak temperature dependence in lightly overdoped cuprates.

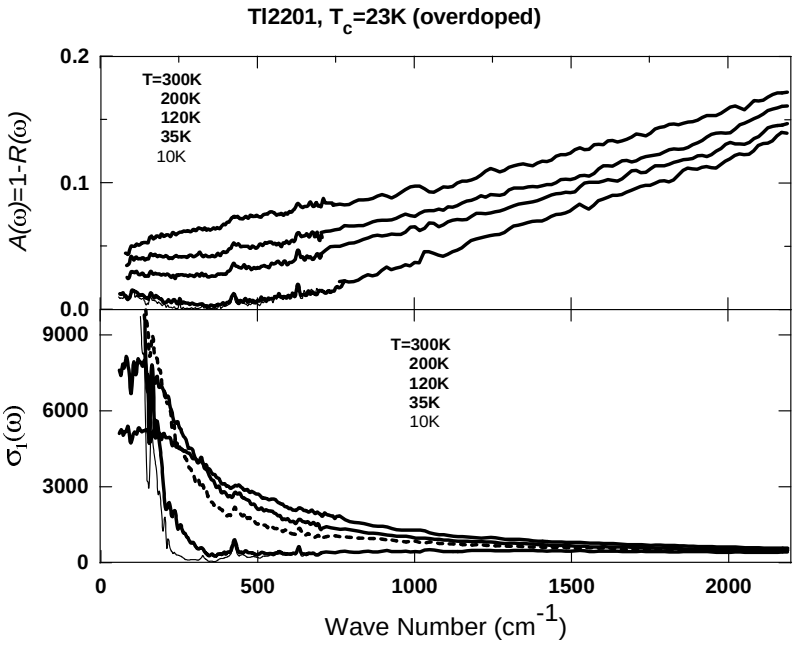

Figure 10. The absorption of strongly overdoped Tl2201 ($T_c = 23$ K) is shown in the top panel and the optical conductivity is shown in the lower panel. The absorption is strongly temperature dependent but no threshold develops at low temperatures. The optical conductivity becomes narrower as temperature decreases but does not show any sharp changes.

4.3. Overdoped cuprates

Since the strongly overdoped regime is not accessible in the Bi2212 or in the YBCO materials, we have chosen Tl2201, (Bi/Pb)2212 and slightly overdoped Bi2212 in order to study this doping regime. In figure 10 we show the data for a strongly overdoped high-T_c superconductor (Tl2201 with $T_c = 23$ K). The raw absorption spectra are qualitatively different from those obtained in optimally doped or underdoped regimes. $A(\omega)$ is temperature dependent over a much broader frequency range. The spectra shift down uniformly as temperature decreases but no sharp features develop. Unfortunately, in this crystal, absorption is already very small in the normal state at $T = 35$ K. It is difficult to determine the exact shape of $A(\omega)$ in the superconducting state. Thus it remains unclear whether the absorption spectra of this crystal show the same threshold structure as those of the less heavily doped materials.

The $\sigma_1(\omega)$ spectra for the strongly overdoped Tl2201 are shown in the bottom panel of figure 10 while $1/\tau(\omega)$ and $m^*(\omega)$ spectra are shown in figure 11. The plasma frequency is $\omega_p = 15\,100$ cm^{-1}. Consistent with the behaviour of the absorption spectra there is no sharp change in the frequency dependence in any of these response functions as the temperature is decreased in the normal state. Instead, the $1/\tau(\omega)$ spectra scale downwards almost parallel to each other. This is in a sharp contrast with the $1/\tau(\omega)$ behaviour in the underdoped regime, where the scattering rate was found to be temperature independent above 1000 cm^{-1}. We also note that the frequency dependence of $1/\tau(\omega)$ for this strongly overdoped material may become superlinear, flattening out at low frequencies. The effective mass $m^*(\omega)$ does not show any pronounced temperature dependence and remains largely

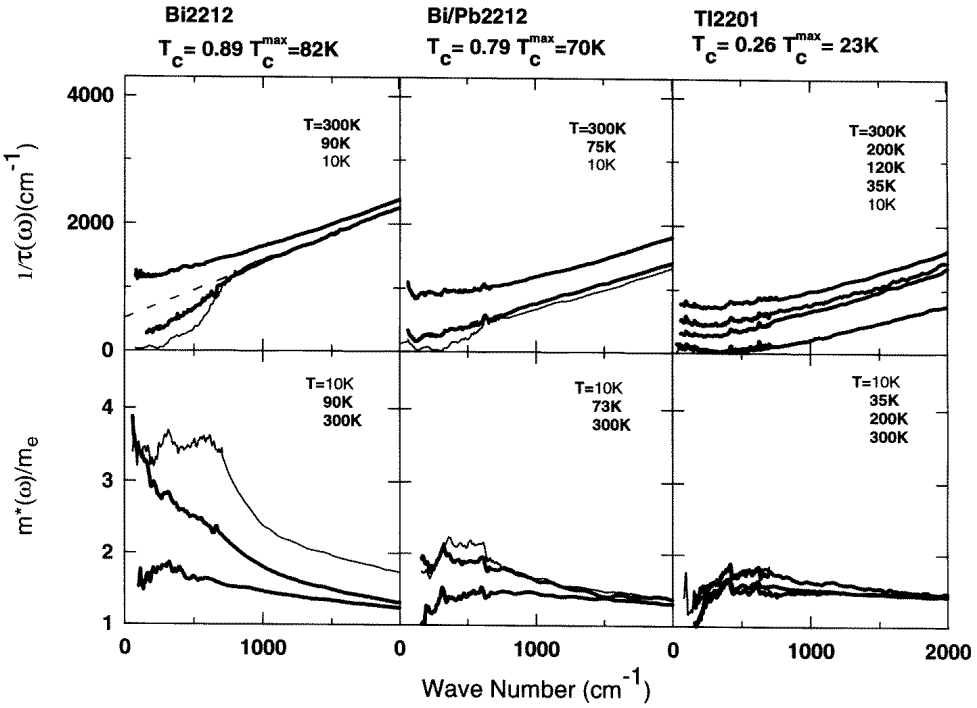

Figure 11. In overdoped samples the scattering rate, shown in the top panels, shows an increasingly strong temperature dependence. As a part of the high-frequency scattering disappears at low temperatures, the low-frequency depression of $1/\tau(\omega)$ and the effective-mass enhancement decreases in magnitude, even in the superconducting state.

flat over the whole frequency region shown. To show the continuity in the evolution of the optical response of the cuprates from underdoped and optimally doped to the strongly overdoped case we plot $1/\tau(\omega)$ and $m^*(\omega)$ spectra for other overdoped samples in the rest of figure 11. These include Bi2212 ($T_c = 82$ K) and (Bi/Pb)2212 ($T_c = 70$ K) annealed in oxygen ($\omega_p = 15\,600$ cm^{-1} for Bi2212 and 16 500 cm^{-1} for (Bi/Pb)2212). As we have noted in the previous section, the $1/\tau(\omega)$ spectrum for the slightly overdoped Bi2212 still shows a weak normal-state pseudogap feature at $T = 90$ K, defined as a downwards deviation from the linear high-frequency behaviour. However, (Bi/Pb)2212 shows no sign of a threshold formation above T_c. While the scattering rate remains close to linear in ω at high frequencies, it seems to gradually pick up a temperature dependence as the doping level is increased from the optimal to overdoped. Also, the absolute value of the scattering rate is gradually suppressed with increased doping.

In the superconducting state the threshold structure seems to weaken as doping is increased towards strong overdoping. Correspondingly, the superconducting-state mass enhancement also becomes weaker. Unfortunately, as in the case of absorption, we cannot unambiguously determine the exact nature of the changes that occur below T_c in either $1/\tau(\omega)$ or $m^*(\omega)$ for the Tl2201 sample with $T_c = 90$ K.

In summary, as the doping level is increased above optimal to overdoped and strongly overdoped levels: (i) no threshold is observed in $1/\tau(\omega)$ at $T > T_c$; (ii) the scattering rate $1/\tau(\omega)$ acquires temperature dependence over a much broader frequency range than in underdoped cuprates; (iii) the frequency dependence of $1/\tau(\omega)$ may become superlinear in

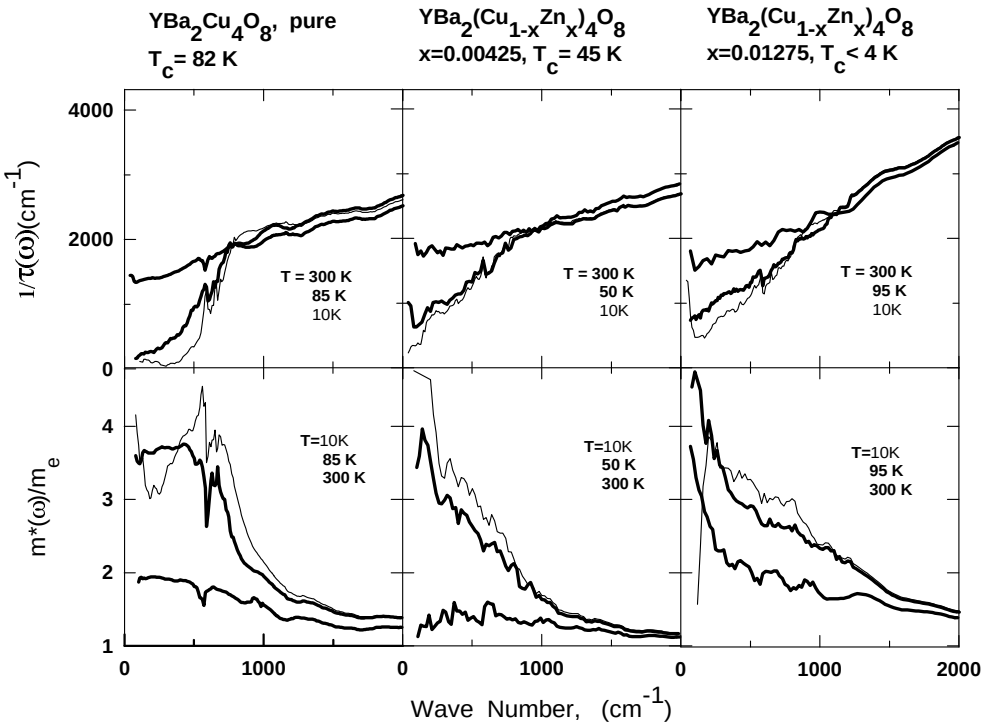

Figure 12. The effect of zinc doping on the *ab*-plane scattering rate for Y124. The left-hand panels show a pure sample while in the middle and right-hand panels results for Y124 with 0.425% and 1.275% of Zn, respectively, are shown. Note the almost complete elimination of the threshold structure at $\sim$700 cm^{-1}.

the strongly overdoped cuprates.

4.4. The effect of zinc doping

In figure 12 we show the spectra of the scattering rate and the effective mass for a pure crystal of Y124 and for two samples containing 0.425% and 1.275% of Zn. As the result of Zn substitution, T_c is suppressed from 82 K in pure crystal down to 45 K in the material with 0.425% of Zn. In the sample with 1.275% Zn, superconductivity is not observed above 4 K. It is believed that Zn substitutes for Cu atoms primarily in the CuO_2 planes.

In the crystals with Zn substitution the scattering rate is enhanced over the whole energy scale. The frequency dependence of $1/\tau(\omega)$ is modified as well. In particular, the threshold structure at $\omega \simeq 600$ cm^{-1} weakens with increasing Zn content. The behaviour of the non-superconducting crystal is in fact very similar to what is observed in the optimally doped samples at $T > T^*$. The principle difference for the Zn-doped underdoped crystals and optimally doped materials is that the threshold structure in $1/\tau(\omega)$ does not appear even below T_c.

At low frequencies we observe an upturn for the $1/\tau(\omega)$ spectra. A similar upturn is also observed for the disordered (Bi/Pb)2212 system and for Tl2201 [73]. It is likely

that this behaviour of the scattering rate could be attributed to incipient localization in the CuO_2 planes initiated by impurities. The upturn becomes stronger as the temperature decreases. We note that the dc properties of these materials, and in particular the temperature dependence of the dc resistivity, are determined by $1/\tau(\omega)$ at $\omega \to 0$. Thus an obvious consequence of the low-frequency upturn would be to reduce the slope of the $d\rho/dT$ dependencies and to create a residual resistivity.

5. Discussion

5.1. General trends in $1/\tau(\omega)$ *data*

With regards to the underdoped cuprates, two distinct features in the $1/\tau(\omega)$ spectra deserve mentioning. First, it must be recognized that $1/\tau(\omega)$ is linear and almost temperature independent at high frequencies. Second, a threshold structure develops at low frequencies and temperatures below T^*. When the doping reaches the optimal level the threshold structure in the ab-plane scattering rate shows up only in the superconducting state. This is accord with the phase diagram where the two curves—those for the pseudogap boundary and the superconducting transition temperature T_c—cross at optimal doping ($T^* \leqslant T_c$). In the overdoped cuprates the threshold structure appears only below T_c and seems to become weaker even in the superconducting state as doping progresses. Unfortunately, the limitations of our experiment do not allow us to say with certainty whether the structure persists in the strongly overdoped materials. The important difference between $1/\tau(\omega)$ for overdoped and underdoped materials is a strong temperature dependence of the high-frequency part of $1/\tau(\omega)$ in the overdoped case.

Table 1. The slopes and zero-frequency intercepts of the high-frequency linear part of $1/\tau(\omega) = \alpha\omega + \beta$ are given in the third and fourth columns. The linear coefficients normalized to the plasma frequency are given in the fifth and sixth columns. The fit was performed over a frequency range from 900–3000 cm^{-1}. The Y124 material is not shown since the high-frequency scattering rate significantly deviates from linearity above 2000 cm^{-1}.

Material	T_c (K)	α	β (cm^{-1})	$4\pi\alpha/\omega_p^2$ ($\mu\Omega$ cm^2)	$4\pi\beta/\omega_p^2$ ($\mu\Omega$ cm)
Y123 (u.d.)	58	1.26 (1.45)	790 (560)	0.34 (0.39)	210 (149)
Y123 (opt.d.)	93.5	0.79 (0.93)	890 (590)	0.15 (0.17)	165 (108)
Bi2212 (u.d.)	67	0.84 (0.91)	1280 (1200)	0.25 (0.27)	377 (352)
Bi2212 (u.d.)	82	0.76 (0.95)	990 (750)	0.19 (0.23)	243 (185)
Bi2212 (opt.d.)	90	0.71 (0.72)	850 (650)	0.17 (0.17)	200 (150)
Bi2212 (o.d.)	82	0.73 (0.77)	890 (550)	0.18 (0.19)	219 (135)
(Bi/Pb)2212 (o.d.)	70	0.63 (0.65)	551 (118)	0.13 (0.14)	117(25)
Tl2212 (o.d.?)	90	0.64 (0.75)	473 (90)	0.16 (0.19)	121 (23)
Tl2212 (o.d.)	23	0.63 (0.54)	337 (−318)	0.17 (0.14)	89 (−84)

The common feature in all of the spectra is the linear dependence of the high-frequency scattering rate. The linear frequency dependence has been seen previously in the scattering rate of the a-axis Y123 both in the optimally doped and underdoped spectra [19, 20]. In table 1 we present the slopes and zero-frequency intercepts of the high-frequency part of the scattering rate obtained by fitting it to a straight line $1/\tau(\omega) = \alpha\omega + \beta$. The results are presented at two temperatures: $T = 300$ K and at the lowest normal temperature (in parentheses).

We note here that the coefficients determined directly from $1/\tau(\omega)$ may be ambiguous since they involve the plasma frequencies that were obtained by integrating the real part of conductivity up to a somewhat arbitrary chosen frequency. However, the same cut-off integration frequency was used for each of the series at all doping levels (1.5 eV for YBCO and 1 eV for Bi2212 and Tl2201). While the absolute value of ω_p obtained in this manner may still be ambiguous, the *changes* in ω_p with doping reflect changes in the carrier density for each of the material series [72]. For these reasons the materials presented in table 1 are grouped by series. Another way to get around the problem of the unknown plasma frequency is to divide the scattering rate by ω_p^2: $4\pi/(\omega_p^2\tau)$. This quantity may be called the 'optical resistivity', or ρ_{opt}, since it has the same functional form as a dc resistivity in a simple Drude model [54]. Since it is directly obtained from the measured complex optical conductivity: $\rho_{opt}(\omega) = \mathrm{Re}(1/\sigma(\omega))$, it may be useful to examine variations of the slope and zero-frequency intercept of $\rho_{opt}(\omega)$ instead of $1/\tau(\omega)$. The corresponding results are listed in the last two columns of table 1.

The result of both approaches is that both α and β seem to decrease with doping for all of the series. However, while the decrease in the slope is insignificant (and may even be inside our error bar estimated to be about 20%), the drop in the intercept, especially its low-temperature value, is dramatic. We also note the large difference between the room-temperature and low-temperature (numbers in parenthesis) intercept values for the overdoped cuprates, which is a result of the intense temperature dependence of the high-frequency part of $1/\tau(\omega)$. The low-temperature intercept even becomes negative for strongly overdoped Tl2201.

The low intercept values for overdoped cuprates suggest that the temperature dependence and the low-frequency threshold of $1/\tau(\omega)$ are closely related. The intense temperature-induced suppression of $1/\tau(\omega)$ over a large frequency range makes the high-frequency background at $T \simeq T_c$ very small. Any further suppression of $1/\tau(\omega)$, similar to that observed in underdoped and optimally doped samples, could potentially produce only a weak feature that would be difficult to detect experimentally.

To conclude this subsection, we make a comparison between our data on the temperature/frequency dependence of the scattering rate and earlier results. For the optimally doped Y123 and Bi2212 samples, microwave and infrared experiments demonstrated that $1/\tau(\omega \to 0)$ drops abruptly below the superconducting transition temperature [74, 75]. A suppression of the scattering rate in the superconducting state was confirmed through transport experiments [76]. These results are consistent with the behaviour of $1/\tau(\omega)$ plotted in figure 9.

In the underdoped regime, the suppression of the scattering rate occurs even in the normal state and thus a comparison can be made with dc resistivity data. In underdoped cuprates the resistivity is a linear function of T for $T > T^*$, but it shows a crossover to a steeper slope at $T < T^*$ [6]. Since dc resistivity is, within a constant factor, the zero-frequency limit of $1/\tau(\omega)$, the crossover behaviour could be completely accounted for with the low-frequency suppression of the scattering rate. We also note that the dc resistivity of underdoped cuprates, at least below 300 K, is determined by the charge dynamics over a relatively small energy range (below the threshold structure) while in the strongly overdoped cuprates, much larger energies are involved. It is not quite clear, however, how the $1/\tau(\omega)$ spectra in the underdoped cuprates will evolve above room temperatures where the dc $\rho_{ab}(T)$ is still increasing with temperature. In particular, it is not clear whether $1/\tau(\omega)$ will remain linear and temperature independent at high frequencies.

5.2. Theoretical models for $1/\tau(\omega)$

There is yet to be a clearly superior theoretical explanation for the peculiar behaviour of the infrared optical response presented in the previous section, but a few models deserve mentioning. We will start here with the models that rely on inelastic scattering processes as the mechanism that determines the frequency and temperature behaviour of the real and imaginary parts of the memory function, and will continue with other models later.

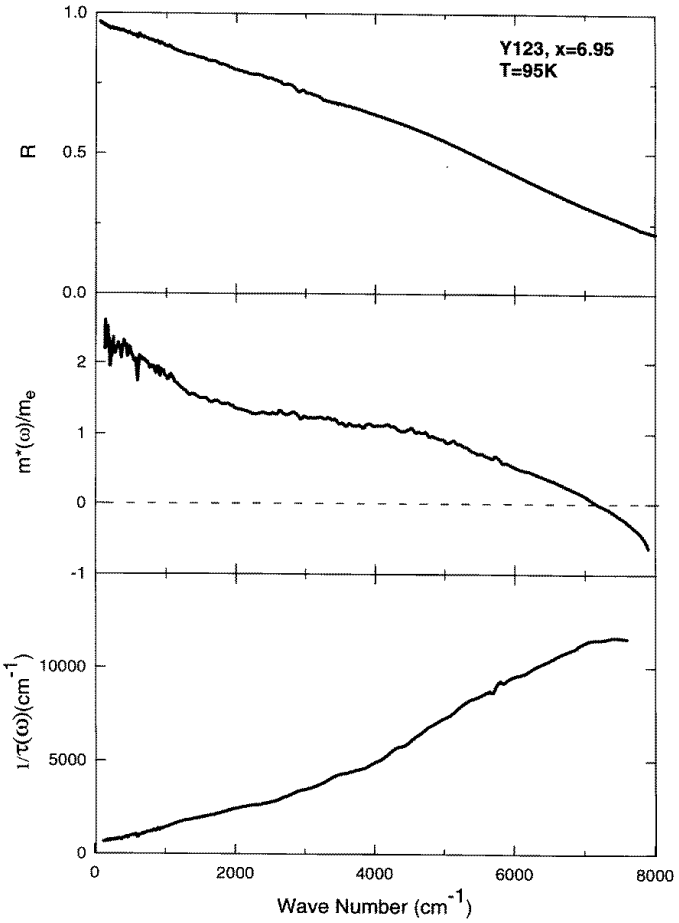

Figure 13. The reflectivity (top panel), the effective mass (middle panel), and the frequency-dependent scattering rate (lower panel) for an optimally doped Y123 crystal shown over a wider frequency range. The temperature is 95 K. The effective mass becomes negative for $\omega > 6000$ cm^{-1} suggesting a breakdown of the validity of the single-component approach due to the onset of an interband transition.

As we have stressed previously, the modelling of the real part of $M(\omega)$ in terms of the carrier scattering only makes sense if there are reasons to believe that the optical response in the energy region under study is predominantly due to mobile carriers (no interband contribution) and that there is only one type of carrier participating in optical excitations (the one-component model). It is not at all clear that these requirements are satisfied in the HTSC cuprates at all frequencies, particularly in the midinfrared range, where some of the

interband transition processes may have energies comparable with the those of the intraband excitations. The situation is complicated further by the fact that these contributions do not have characteristic sharp features which would facilitate their separation. As an example, a typical frequency dependence of the room-temperature *ab*-plane complex memory function $M(\omega)$, in the functional form of $1/\tau(\omega)$ and $m^*(\omega)$, is shown in figure 13 on a large frequency scale for Y123 ($x = 6.95$) material ($\boldsymbol{E}\|\boldsymbol{a}$). Evidence for the interband process comes from, for example, $m^*(\omega)$ being negative [77] at $\omega > 8000$ cm^{-1}.

Nevertheless, there are reasons to believe that the carrier scattering approach can be used at frequencies below 2000–3000 cm^{-1} for which we have presented data in section 4. First, the conductivity is observed to be temperature dependent [78] at $\omega <$ 2000–3000 cm^{-1}, and it is natural to assign the temperature-dependent part to the 'free'-carrier contribution; second, as was noted earlier by Thomas *et al* [15], the number of carriers that one obtains using the sum-rule analysis for the real part of the optical conductivity is consistent with estimates from chemical valence arguments for the carrier density provided that the sum rule is taken up to about 8000 cm^{-1}.

Therefore the carrier scattering mechanism is at least a plausible mechanism for the optical response in HTSC at frequencies less than 2000–3000 cm^{-1}. Below we will outline some approaches that are based on carrier scattering mechanisms as well as some problems associated with them.

The first approach is electron–phonon scattering [56]. While this model qualitatively reproduces the gap-like depression in $1/\tau(\omega)$ at low temperatures (see, for example, calculations presented in figures 3 and 4), it is not nearly as sharp as that seen in the experimental data. An even more severe problem is the absence of the predicted temperature dependence of $1/\tau(\omega)$ at high frequencies. A signature of the electron–phonon theories is their prediction of significant temperature-induced changes (proportional to k_BT at high temperatures). Furthermore, as discussed in section 3, within the electron–boson scattering scenario, the characteristic temperature below which a low-frequency depression in $1/\tau(\omega)$ occurs is determined by the high-energy cut-off of the bosonic spectrum $\mathcal{A}_{tr}(\Omega)$. The experimental fact is that the characteristic temperature in the cuprates, T^*, depends on the doping level. This is inconsistent with the electron–phonon scenario, since the phonon cut-off is doping independent. Thus we believe that the electron–phonon scattering model fails to reproduce the essential features of the experimental data for underdoped cuprates.

It is still possible, however, that phonons play some role in the mechanism responsible for the experimentally observed behaviour of $1/\tau(\omega)$, but in a more unconventional way. We note in this respect that the frequency scale in the spectra of $1/\tau(\omega)$ associated with the pseudogap state, which does not significantly change with doping, coincides remarkably well with the high-frequency cut-off energy of the phonon density of states in HTSC [79].

More generally, a serious defect of all of the models that employ scattering of electrons by bosonic excitations to describe the optical response of underdoped HTSC is their failure to account for the observed behaviour in the high-frequency part of the $1/\tau(\omega)$ spectra. As discussed in section 4, underdoped cuprates do not show any temperature dependence in $1/\tau(\omega)$ at $\omega >$ 700–800 cm^{-1}. On the other hand, in section 3 we saw that scattering of electrons by any temperature-independent bosonic spectrum leads to a strong temperature dependence of $1/\tau(\omega)$ at high frequencies. The only way to get around this contradiction is to assume that the boson spectral function $\mathcal{A}_{tr}(\Omega)$ is also a function of *temperature*: $\mathcal{A}_{tr}(\Omega, T)$. In this case, if the absolute value of $\mathcal{A}_{tr}(\Omega, T)$ scales properly with temperature, it may account for the observed temperature-independent scattering rate at high frequencies. The phonon density of states does not show any such changes [79].

One of the mechanisms that may yield a temperature-dependent $\mathcal{A}(\omega)$ function is the

scattering of charge carriers on local fluctuations towards an antiferromagnetic order. The energy scale associated with spin fluctuations is measured [80] to be of the order of 50 meV. The features in the scattering rate spectra that we observe in the pseudogap state are on the same energy scale, supporting such models. This mechanism would also provide a qualitative explanation for the doping dependence of the pseudogap.

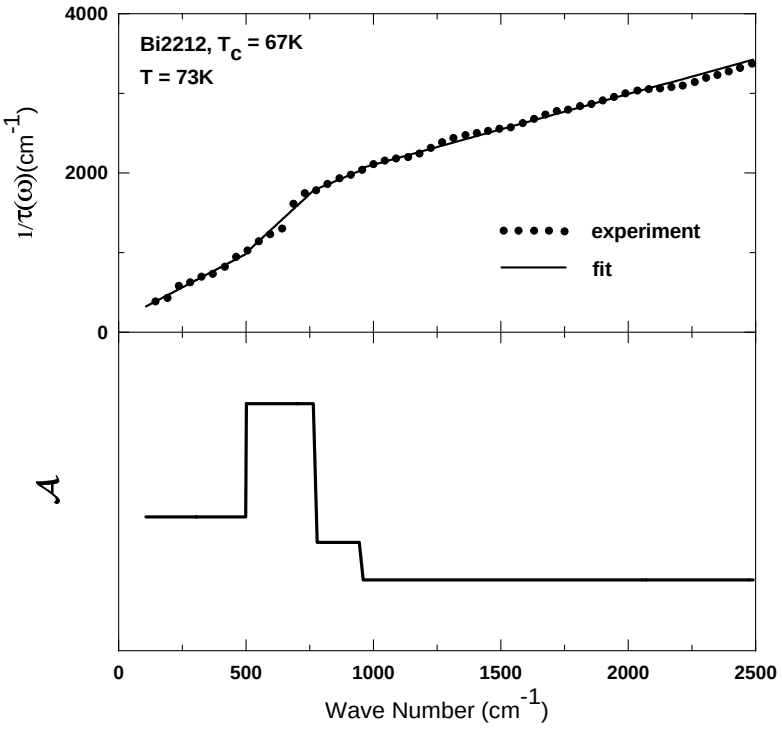

Figure 14. Top panel: the scattering rate above T_c in the pseudogap state is approximated by straight-line segments. Bottom panel: the slopes of the straight segments are plotted as a function of frequency.

Finally, we can roughly estimate the boson spectral function that is needed to obtain the threshold structure in $1/\tau(\omega)$ in the pseudogap state at $T < T^*$. This estimate can be obtained by inverting the lowest-temperature normal-state experimental results for $1/\tau(\omega)$ using Allen's expression (equation (14)). The complete inversion formula can be written as $\mathcal{A}(\omega) = (1/\omega)(\mathrm{d}/\mathrm{d}\omega)[\omega^2(\mathrm{d}/\mathrm{d}\omega)(1/\tau(\omega))]$ [81]. Since the process of numerical differentiation greatly amplifies the noise level of our spectra, we have chosen the following approach to minimize the added noise. The experimentally obtained $1/\tau(\omega)$ for underdoped Bi2212 was fitted with four straight lines, as shown in figure 14 and then the inversion formula was applied to the resulting artificial spectrum composed of the straight pieces. In this scheme, the exact inversion formula reduces to the first derivative, that is the slope of the straight lines. The resulting $\mathcal{A}_{tr}(\Omega)$ spectrum is shown in the bottom panel of figure 14. Obviously the rather crude approximation of the experimental curve prevents us from observing any fine details of the spectrum. The significant result is, however, that an intense peak in $\mathcal{A}_{tr}(\Omega)$ at 500–700 cm^{-1}, superimposed on a broad background, is needed to account for the behaviour of the scattering rate in the pseudogap state if one adopts an electron–boson scattering model.

We note that at least some of the current electron–electron scattering models suffer the same problems as the electron–boson ones—namely, they cannot account for the weak or completely absent temperature dependence of $1/\tau(\omega)$ spectra in underdoped cuprates at high frequencies. In the conventional Fermi-liquid theory, for example, the electron–electron scattering rate is proportional to $(\hbar\omega)^2 + (\pi k_B T)^2$, that is the frequency and temperature dependences of the scattering rate 'mirror' one another [82]. Another example of this type of mirroring is provided by the heavy-fermion compound URu_2Si_2 [83] or the perovskite Sr_2RuO_4 [84]. In both cases a scaling of $\hbar\omega = 2k_B T$ collapses the dc resistivity curve onto the frequency-dependent scattering rate curve. This is in contrast to the experimental observations for underdoped cuprates where a significant frequency dependence, but no temperature dependence, was observed at frequencies above 1000 cm^{-1}. Other Fermi-liquid-type models, such as the nested Fermi-liquid (NFL) model or the marginal Fermi-liquid (MFL) model, also predict a significant temperature dependence at high frequencies [67, 58]. For example, the main assumption of the phenomenological MFL model is that the scattering rate varies as $1/\tau(\omega, T) = \alpha\omega + \beta T$ where α and β are constants of the order of unity. It is clear that in the underdoped materials $1/\tau$ does not follow this behaviour since $\beta = 0$, i.e. there is no temperature dependence associated with the linear-in-frequency scattering rate. As we have seen, a temperature dependence of the scattering rate does develop, but only in optimally doped and overdoped materials.

We note that from a completely different point of view, the two-component model of optical conductivity [85] where the infrared conductivity is divided into a free-carrier and a midinfrared component, these observations imply that the midinfrared component is temperature independent in underdoped materials.

Some hints regarding the microscopic origin of the scattering mechanism in HTSC can be obtained from the analysis of impurity effects. As was shown in section 4, the effect of Zn doping was not just the introduction of an additional frequency-independent term in $1/\tau(\omega)$ spectra. Zinc substitution also modifies the frequency dependence of the scattering rate suggesting that *inelastic* processes are affected by Zn as well. The *c*-axis results obtained for the sample with 0.425% Zn reveal a *complete suppression* of the pseudogap [68]. The effect of Zn on the *c*-axis pseudogap is similar to the one observed in the spin–lattice relaxation time $1/TT_1$ [86]. The similar concentrations of Zn in ceramic pellets of Y124 completely suppress the pseudogap feature in the temperature dependence of $1/TT_1$, despite the fact that the behaviour of the Knight shift remains unchanged from that of a pure sample. The results obtained from crystals with Zn substitution strongly suggest that spin fluctuations may be involved or may even be the dominant mechanism of scattering in underdoped cuprates.

There are several other theoretical models that attempt to explain the pseudogap phenomenon from different assumptions.

The model due to Emery and Kivelson [87] predicts that the low carrier density in the underdoped regime may result in pairing without pair–pair coherence at temperatures well above the actual T_c, thus producing a pseudogap. As the temperature is lowered the phase coherence is established, leading to bulk superconductivity. This model would provide an explanation for the lack of dramatic changes upon crossing into the superconducting state, which is consistent with our optical experiments as well as ARPES measurements. However, it is not quite clear why the high-frequency onset energy of the optical pseudogap does not change as a function of doping while T^* and T_c do.

In the spin–charge separation picture [57], spin singlets form at T^*, giving rise to a spin gap while the charge carriers, holes which are bosons, Bose condense at the superconducting transition [88–91]. Other models invoke a spin-density wave [92, 93] in the context of

a normal Fermi liquid to form a gap in the spin excitations which are the predominant scatterers of the charge carriers.

5.3. The effect of Zn doping

As a small fraction of Cu is substituted for with Zn, the optical response of underdoped Y124 changes dramatically. Contrary to what is seen for the underdoped samples in the pseudogap state or the optimally doped sample in the superconducting state, there is no structure in the scattering rate either above or below T_c. These results suggest that the temperature characterizing the pseudogap state T^* can be very small and definitely much lower than T_c. We note that a similar effect may be seen for overdoped cuprates. Therefore we suggest that the addition of Zn may have an effect similar to the overdoping of Y124 compounds.

The normal-state plasma frequency is not affected by Zn substitution. Indeed, as was demonstrated by Puchkov *et al* [72], overdoping does not lead to any significant changes in the value of the in-plane plasma frequency. At the same time, overdoped compounds usually show a higher dc conductivity than their underdoped or optimally doped counterparts. That is not the case for the Y124 material with Zn where the conductivity $\sigma_a(\omega \rightarrow 0)$ is reduced. However, this may simply reflect the fact that Zn is put directly in the CuO_2 planes and this inevitably causes additional impurity scattering. The latter effect is so strong that crystals with 1.25% of Zn show evidence for a charge-carrier localization behaviour in the optical conductivity. This point will be addressed in detail elsewhere.

It is critical to determine whether the effects observed for the Y124 crystals on Zn substitution are unique for this specific impurity or whether other types of disorder would produce similar results.

5.4. The relation between the ab-plane and c-axis pseudogap

A comparison of *a*-axis results for Y123 materials with earlier *c*-axis data [25, 26] suggests that the pseudogap directly observed in the *c*-axis conductivity at $T < T^*$ is necessarily accompanied by a suppression of the in-plane $1/\tau(\omega)$ at low frequencies. Indeed, the threshold feature in $1/\tau_a(\omega)$ is found for underdoped crystals at $T < T^*$ *only* when the spectrum of $\sigma_c(\omega)$ exhibits a pseudogap. The suppression of the pseudogap in $\sigma_c(\omega)$, either by an increase of temperature above T^*, or by an increase of the carrier density from $x = 6.6$ to $x = 6.95$ in Y123, or by the substitution for Cu with Zn in underdoped Y124 [68], restores the nearly linear frequency dependence of the in-plane scattering rate. Therefore, we conclude that the same microscopic mechanism leads to the opening of the pseudogap in the interplane response of YBCO crystals *and* the low-frequency anomalies in the lifetime effects within the CuO_2 planes.

It is interesting to note that the frequency shape of the *c*-axis conductivity is somewhat similar to the bosonic spectral function, shown in figure 14, that is needed to reproduce the *in-plane* behaviour of $1/\tau(\omega)$. This suggests that there may be an intricate connection between the two.

5.5. The superconducting state

One of the most striking features of the curves, in our view, is how closely the $1/\tau$ curves for the underdoped cuprates in the superconducting state resemble those in the pseudogap state. It is useful to compare the energy scales for the various experiments that reveal the

presence of a pseudogap.

The maximum gap seen in the ARPES experiment is about $2\Delta = 360$ cm^{-1} (45 meV) whereas the *c*-axis conductivity (in YBCO) shows an onset at $\sim$200 cm^{-1} (25 meV) rising to a plateau at 360 cm^{-1} (45 meV). The *ab*-plane $1/\tau$ scale is considerably higher with the steepest part of the curve at $\sim$500 cm^{-1} (62 meV) merging with the high-frequency linear curve at around 750 cm^{-1} (93 meV) in all of the materials studied. Another high-energy scale is the energy range of the depression of the *c*-axis conductivity at the superconducting transition—of the order of or larger than 600 cm^{-1}.

Thus it appears to us that the energy scales associated with the pseudogap and with the superconducting state are different. In Y124 crystals with Zn substitution, superconductivity persists while the pseudogap is suppressed. We also note that in all of the samples we find finite absorption extending down to the lowest frequencies. In an s-wave superconductivity scenario, this absorption implies a very anisotropic superconducting gap. As for the d-wave gap models, our data may be consistent with the theoretical predictions [94–96] only if one assumes a significant number of impurities present in the crystals. This assumption is, however, inconsistent with the linear penetration depth observed in the high-quality YBCO crystals used in this work [97, 98].

Although changes in $1/\tau(\omega)$ upon crossing into the superconducting regime in the optimally doped cuprates are apparently dramatic, this may simply be due to the simultaneous formation of the pseudogap and superconducting condensate. Also, as noted above, it is only in the *c*-axis conductivity that we see evidence of a larger energy scale associated with the superconducting state [26].

In the superconducting state, the spectra of the effective mass are remarkably similar in all of the crystals that we have studied. In particular, the absolute value of $m^*(\omega \to 0)$ is about 4 both in Y123 and in Y124 materials. As noted in section 3, the zero-frequency extrapolation of the effective mass gives a square of a ratio of the total plasma frequency, ω_p, to the plasma frequency of the superconducting condensate, ω_{ps}. This value is in good agreement with the results obtained directly from the use of the sum-rule analysis of $\sigma_1(\omega)$ or from an analysis of the imaginary part of the conductivity. The fact that the zero-frequency extrapolations of the effective mass are roughly the same, $m^*(\omega \to 0) \simeq 3.5$–4, for all of the underdoped materials suggests that the superfluid condensate density scales with the total carrier density in the underdoped cuprates. Therefore, we conclude that there are no pair-breaking effects in the pseudogap state. However, as doping is increased above optimal, the mass enhancement becomes weaker, which indicates a decrease in the superfluid density. This behaviour is in agreement with the earlier μSR results [99–101].

5.6. The phase diagram and the comparison with c-axis data

In figure 1 we show a phase diagram where the characteristic temperatures T^* (determined from the *c*-axis conductivity) and T_c for several different samples from the YBCO family are plotted as a function of superfluid density $\omega_{ps}^2 = n_s/m^*$ in the CuO_2 planes. The superfluid density is obtained from the optical conductivity as described in section 3. Our choice of superfluid density rather than ω_p^2 of the normal-state carriers is governed by the fact that the former quantity could be determined unambiguously from the real part of the *ab*-plane infrared conductivity. From underdoped to optimally doped regimes the critical temperature scales with the superfluid density in the CuO_2 planes, and the T_c-points for $YBa_2Cu_3O_{6.6}$ and $YBa_2Cu_3O_{6.95}$ crystals fall on the universal dependence first proposed by Uemura *et al* [99, 100]. T_c of Y124 is 20% above the universal line. The T_c versus n_s/m^* boundary in the phase diagram is well defined since both T_c and n_s/m^* could be determined very

accurately. However, the T^* versus n_s/m^* boundary cannot be determined with same high precision since the uncertainty in T^* is about 20–30 K, based on the c-axis conductivity data. The four T^*-points correspond to the following crystals: $T^* = 300$ K—Y123 crystal with $x = 6.6$; $T^* = 180$ K—Y123 with $x = 6.7$ [49]; $T^* = 140$ K—Y124 crystal, and for Y123 with $x = 6.95$, $T^* = T_c = 93.5$ K. The variation of T^* between the different YBCO samples significantly exceeds the error in the absolute value of T^*. So far crystals with oxygen contents less than $x = 6.5$ have not been investigated in detail. Thus it is unclear whether the pseudogap temperature continues to grow as one approaches the insulating region in the phase diagram or whether it saturates at the level of 300–400 K.

5.7. Open questions

At the time of writing this survey of the ab-plane pseudogap phenomenon, there remain many open questions. The first question that must be addressed is that of whether or not the pseudogap state is generic among all high-T_c materials. In particular, does anything similar exist for non-cuprate superconductors such as BKBO or $RENi_2B_2C$?

It has been suggested that the pseudogap is a manifestation of interlayer coupling and is specific to the double-layer materials such as YBCO and Bi2212 [71]. Support for this view comes from NMR measurements, which show a rather weak depression of the magnetic susceptibility in La214 in the temperature range where the transport data show evidence of a strong suppression of the scattering. As we have seen from our presentation of the data for overdoped single-plane Tl2201 samples, the ab-plane $1/\tau(\omega)$ curves look similar to those of the two-plane materials *in the superconducting state*.

Experimental optical data exist for the one-plane La214 material [102, 40, 103] which, in the underdoped regime, shows a very strong depression in $1/\tau(\omega)$ at low temperatures which is consistent with the pseudogap picture. However, one must be cautious at this stage since the data from various laboratories show considerable variation as regards the magnitude of the effect. In some cases, the structure in the reflectivity is so strong that it produces an unphysical singularity in the $1/\tau(\omega)$ curves [40]. More work on a range of samples must be done for this system. Similar strong features are seen for the electron-doped $Nd_{2-x}Ce_xCuO_4$ material [103].

It has been suggested that the one-component model of charge transport in the cuprates is particularly unsuited for the La214 system where, at least at low doping levels, $\sigma(\omega)$ shows a separate midinfrared band [104] rather than a smooth free-carrier band with excess conductivity at high frequencies. It is also known that at very low doping levels, in the insulating state, there is a separate band or several bands [105, 106] and a one-component picture is clearly inappropriate.

Another important effect that needs to be examined is the role of impurities. We have seen that Zn has the effect of destroying the pseudogap in Y124, both in the c-axis $\sigma_1(\omega)$ and in the ab-plane $1/\tau(\omega)$ curves which acquire a frequency dependence similar to what is seen in the overdoped materials. Zn is an impurity that has a strong effect on T_c and a systematic study of the influence of Zn may help us to isolate its effect on T^*, the onset temperature of the pseudogap phase, and T_c, the onset temperature of superconductivity.

Phonons play an important, if perhaps subsidiary, role in high-temperature superconductivity. As we have seen in section 3, the standard electron–phonon mechanism predicts a temperature-dependent $1/\tau(\omega)$ at all frequencies whereas the observations in the pseudogap state show a temperature-independent high-frequency $1/\tau(\omega)$. On the other hand, the frequency range of the steepest rise of $1/\tau(\omega)$ falls in the oxygen-mode region of the phonon spectrum and seems to vary little with temperature, chemical composition or

doping. This inertness of the pseudogap frequency suggests that phonons may be involved in some indirect way.

One process that affects the ab-plane conductivity in all high-T_c materials is the coupling of the ab-plane electrodynamic response to c-axis LO phonons [23, 22, 107]. To separate this process from other processes, it is necessary to measure the in-plane optical response on the ac-face of an underdoped crystal where the LO_c coupled structure vanishes [23].

The signature of the pseudogap state of YBCO materials is that the in-plane conductivity is enhanced whereas the interplane conductivity is suppressed. It is important to find out whether this is manifested by other cuprates.

6. Conclusions

In our review of the recent optical data, we see that there is a universal depression of the real part of the memory function $M'(\omega)$, or $1/\tau(\omega)$, below an energy of the order of 700–800 cm^{-1} in all underdoped materials below a characteristic temperature T^*. At the optimal doping level $T_c \simeq T^*$ and in the strongly overdoped regime the gap-like depression is not seen. While the high-frequency $1/\tau(\omega)$ was found to be temperature independent for the underdoped cuprates, an obvious temperature dependence is seen for the strongly overdoped cuprates. We believe that these optical results add to the growing evidence for the existence of a normal-state pseudogap in the physical response function of the underdoped HTSC.

While intense theoretical work has been done with the aim of explaining the observed phenomenon, none of it has been completely successful. It is necessary for any theoretical model to explain not only the formation of the gap in the ab-plane response, but also a wealth of phenomena, such as the c-axis transport and the remarkable temperature dependencies that are observed, both for the c-axis pseudogap as well as the ab-plane response.

Acknowledgments

The authors wish to acknowledge a collaboration with the following crystal-growing groups, without whom this work would not have been possible: the Bi2212 single crystals were grown at Stanford University by P Fournier and A Kapitulnik; the Tl2201 single crystals were grown by N N Kolesnikov of the Institute of Solid State Physics, Russia, and S Doyle and A M Hermann of the University of Colorado, Boulder; the detwinned Y123 crystals came from our long-time collaborators, R Liang, D A Bonn and W H Hardy at the University of British Columbia; the Y124 single crystals were grown by Bogdan Dabrowski at the Northern Illinois University.

We are very grateful to C C Homes, T Rõõm and T Startseva for allowing us to use their experimental data in this paper.

The authors also wish to acknowledge illuminating discussions with A A Abrikosov, P B Allen, A J Berlinsky, D A Bonn, N Bontemps, J P Carbotte, J C Cooper, O V Dolgov, R C Dynes, V J Emery, W N Hardy, C C Homes, M Julien, K Kallin, S A Kivelson, R B Laughlin, P A Lee, A G Loeser, J W Loram, F Marsiglio, A J Millis, D Pines, M Strongin, Z-X Shen, D van der Marel, and Y Uemura.

This work was supported by the Canadian Institute of Advanced Research (CIAR) and the Natural Sciences and Engineering Research Council of Canada.

References

[1] Warren W W Jr, Walstedt R E, Brennert G F, Cava R J, Tycko R, Bell R F and Dabbagh G 1989 *Phys. Rev. Lett.* **62** 1193
[2] Yoshinari Y, Yasuoka H, Ueda Y, Koga K and Kosuge K 1990 *J. Phys. Soc. Japan* **59** 3698
Alloul H, Ohno T and Mendels P 1990 *J. Less-Common Met.* **164–165** 1022
[3] Gurvitch M and Fiory A T 1987 *Phys. Rev. Lett.* **59** 1337
[4] Bucher B, Steiner P, Karpinski J, Kaldis E and Wachter P 1993 *Phys. Rev. Lett.* **70** 2012
[5] Batlogg B, Hwang H Y, Takagi H, Cava R J, Kao H L and Kwo J 1994 *Physica* C **235–240** 130
[6] Ito T, Takenaka K and Uchida S 1993 *Phys. Rev. Lett.* **70** 3995
[7] Walkes D R, Carrington A, Mackenzie A P and Cooper J R, unpublished, cited in
Gabay M and Lederer P 1993 *Phys. Rev. Lett.* **47** 14 462
[8] Rossat-Mignod J, Regnault L P, Vettier C, Bourges P, Burlet P, Bossy J, Henry J Y and Lapertot G 1991 *Physica* C **185–189** 86
Tranquada J M, Gehring P M, Shirane G, Shamoto S and Sato M 1992 *Phys. Rev.* B **46** 5561
[9] Loram J W, Mirza K A, Cooper J R and Liang W Y 1994 *J. Supercond.* **7** 261
[10] Friedl B, Thomsen C and Cardona M 1990 *Phys. Rev. Lett.* **76,** 1107
[11] Litvinchuk A P, Thomsen C and Cardona M 1992 *Solid State Commun.* **83** 343
[12] Cooper S L, Klein M V, Pazol B G, Rice D M and Ginsberg D M 1988 *Phys. Rev.* B **37** 5920
[13] Slakey F, Klein M V, Rice J P and Ginsberg D M 1990 *Phys. Rev.* B **42** 2643
[14] Reedyk M, Bonn D A, Garrett J D, Greedan J E, Stager C V, Timusk T, Kamarás K and Tanner D B 1988 *Phys. Rev.* B **38** 11 981
[15] Thomas G A, Orenstein J, Rapkine D H, Capizzi M, Millis A J, Bhatt R N, Schneemeyer L F and Waszczak J V 1988 *Phys. Rev. Lett.* **61** 1313
[16] Orenstein J, Thomas G A, Millis A J, Cooper S L, Rapkine D, Timusk T, Schneemeyer L F and Waszczak J V 1990 *Phys. Rev.* B **42** 6342
[17] Kamarás K, Herr S L, Porter C D, Tache N Tanner D B, Etemad S, Venkatesan T, Chase E, Inham A, Wu X D, Hegde M S and Dutta B 1990 *Phys. Rev. Lett.* **64** 84
[18] van der Marel D, Habermeier H-U, Heitmann D, König W and Wittlin A 1991 *Physica* C **176** 1
[19] Schlesinger Z, Collins R T, Holtzberg F, Feild C, Blanton S H, Welp U, Crabtree G W, Fang Y and Liu J Z 1990 *Phys. Rev. Lett.* **65** 801
[20] Rotter L D, Schlesinger Z, Collins R T, Holtzberg F, Feild C, Welp U, Crabtree G W, Liu J Z, Fang Y Vandervoort K G and Flesher S 1991 *Phys. Rev. Lett.* **67** 2741
[21] Schlesinger Z, Collins R T, Rotter L D, Holtzberg F, Feild C, Welp U, Crabtree G W, Liu J Z, Fang Y, Vandervoort K G and Flesher S 1994 *Physica* C **235–240** 49
[22] Timusk T, Porter C D and Tanner D B 1991 *Phys. Rev. Lett.* **66** 663
[23] Reedyk M and Timusk T 1992 *Phys. Rev. Lett.* **69** 2705
[24] Timusk T, Herr S L, Kamarás K, Porter C D, Tanner D B, Bonn D A, Garrett J D, Stager C V, Greedan J E and Reedyk M 1988 *Phys. Rev.* B **38** 6683
[25] Homes C C, Timusk T, Liang R, Bonn D A and Hardy W N 1993 *Phys. Rev. Lett.* **71** 1645
[26] Basov D N, Timusk T, Dabrowski B and Jorgensen J D 1994 *Phys. Rev.* B **50** 3511
[27] Tajima S, Schützmann J and Miyamoto S 1995 *Solid State Commun.* **95** 759
[28] Leggett A J 1994 *Braz. J. Phys.* B **50** 496
[29] Homes C C, Timusk T, Liang R, Bonn D A and Hardy W H 1995 *Physica* C **254** 265
[30] Basov D N, Mook H A, Dabrowski B and Timusk T 1995 *Phys. Rev.* B **52** R13 141
[31] Kumar N, Lee P A and Shapiro B 1990 *Physica* A **168** 447
[32] Kumar N and Jayannavar A M 1992 *Phys. Rev.* B **50** 438
[33] Rojo A G and Levin K 1993 *Phys. Rev.* B **48** 16 861
[34] Graf M J, Rainer D and Sauls J A 1995 *Phys. Rev.* B **47** 12 089
[35] Ioffe L B, Larkin A I, Varlamov A A and Yu L 1993 *Phys. Rev.* B **47** 8936
[36] Nyhus P, Karlow M A, Cooper S L, Veal B and Paulikas A P 1994 *Phys. Rev.* B **50** 13 898
[37] Clarke D G, Strong S P and Anderson P W 1995 *Phys. Rev. Lett.* **74** 4499
[38] Alexandrov A S, Kabanov V V and Mott N F 1996 unpublished
[39] Takigawa M, Reyes A P, Hammel P C, Thompson J D, Heffner R H, Fisk Z and Ott K C 1991 *Phys. Rev.* B **43** 247
[40] Uchida S, Tamasaku K and Tajima S 1996 *Phys. Rev.* B **53** 14 558
[41] Reedyk M 1996 unpublished
[42] Marshall D S, Dessau D S, Loeser A G, Park C H, Shen Z-X, Matsuura A Y, Eckstein J N, Bozovik I,

Fornier P, Kapitulnik A, Spicer W E and Shen Z-X 1996 *Phys. Rev. Lett.* **76** 4841
[43] Loeser A G, Shen Z-X, Dessau D S, Marshall D S, Park C H, Fornier P and Kapitulnik A 1996 *Science* **273** 325
[44] Ding H, Tokoya T, Campuzono J C, Takahashi T, Randeria M, Norman M R, Mochiku T, Kadowaki K and Giapintzakis J 1996 *Nature* **382** 51
[45] Dabrowski B 1996 unpublished
[46] Liang Ruxiang, Dosanih P, Bonn D A, Baar D J, Carolan J E and Hardy W N 1992 *Physica* C **195** 51
[47] Dabrowski B, Zhang K, Pluth J J, Wagner J L and Hinks D G 1992 *Physica* C **202** 271
[48] Fournier P, Kapitulnik A and Marshall A F 1996 *Physica* C **257** 291
Kolesnikov N N, Kulakov M P, Molchanov V N, Schegolev I F, Shibaeva R P, Simonov V I, Tamazyan R A and Vyaselev O M 1995 *Physica* C **242** 385
[49] Homes C C, Reedyk M A, Crandles D A and Timusk T 1993 *Appl. Opt.* **32** 2976
[50] Timusk T and Tanner D B 1989 *Infrared Properties of High T_c Superconductors (Physical Properties of High Temperature Superconductors I)* ed D M Ginsberg (Singapore: World Scientific) p 339
[51] Romberg H, Nucker N, Fink J, Wolf T, Xi X X, Kock B, Geserich H P, Durrler M, Assmus W and Gegenheimer B 1990 *Z. Phys.* B **78** 367
[52] Humliček J, Schmidt E, Bočánek L, Carriga M and Cardona M 1990 *Solid State Commun.* **73** 127
[53] Cooper S L, Reznik D, Kotz A, Karlow M A, Liu R, Klein M V, Lee W C, Giapintzakis J, Ginsberg D M, Veal B W and Pulikas A P 1993 *Phys. Rev.* B **47** 8233
[54] Ashcroft N W and Mermin N D 1976 *Solid State Physics* (Philadelphia, PA: Saunders College)
[55] Abrikosov A A, Gorkov L P and Dzyaloshinski I E 1975 *Methods of Quantum Field Theory in Statistical Physics* (New York: Dover)
[56] Shulga S V, Dolgov O V and Maksimov E G 1991 *Physica* C **178** 266
[57] Anderson P W 1987 *Science* **235** 1196
[58] Schmitt-Rink S, Varma C M and Ruckenstein A E 1988 *Phys. Rev. Lett.* **60** 2793
[59] Emery V J and Kivelson S A 1995 *Phys. Rev. Lett.* **74** 3253
[60] Allen P B and Mikkelsen J C 1976 *Phys. Rev.* B **15** 2953
[61] Mori H 1965 *Prog. Theor. Phys.* **34** 399
[62] Götze W and Wölfe P 1972 *Phys. Rev.* B **6** 1226
[63] Allen P B 1971 *Phys. Rev.* B **3** 305
[64] Webb B C, Sievers A J and Mihalisin T 1986 *Phys. Rev. Lett.* **57** 1951
[65] Dolgov O V and Shulga S V 1995 *J. Supercond.* **8** 611
[66] Collins R T, Schlesinger Z, Holtzberg F, Chaudhari P and Feild C 1990 *Phys. Rev. Lett.* **39** 6571
[67] Rieck C T, Little W A, Ruvalds J and Virosztek A 1995 *Phys. Rev.* B **51** 3772
[68] Basov D N, Liang R, Dabrowski B, Bonn D A, Hardy W N and Timusk T 1996 unpublished
[69] Puchkov A V, Fournier P, Basov D N, Timusk T, Kapitulnik A and Kolesnikov N N 1996 *Phys. Rev. Lett.* **77** 3212
[70] Millis A J, Sachdev S and Varma C M 1988 *Phys. Rev.* B **37** 4975
[71] Millis A J, Monien H and Pines D 1990 *Phys. Rev.* B **42** 167
[72] Puchkov A V, Fournier P, Timusk T and Kolesnikov N N 1996 *Phys. Rev. Lett.* **77** 1853
[73] Puchkov A V and Timusk T 1996 unpublished
Puchkov A V, Timusk T, Doyle S and Hermann A M 1995 *Phys. Rev.* B **51** 3312
[74] Bonn D A, Dosanih P, Liang R and Hardy W N 1992 *Phys. Rev. Lett.* **68** 2390
[75] Romero D B, Porter C D, Tanner D B, Forro L, Mandrus D, Mihaly L, Carr G L and Williams G P 1992 *Phys. Rev. Lett.* **68** 1590
[76] Yu R C, Salamon M B, Lu J P and Lee W C 1992 *Phys. Rev. Lett.* **69** 1431
[77] Since an interband transition can be roughly modelled by an oscillator centred at ω_i, the imaginary part of the conductivity is negative below ω_i.
[78] Romero *et al* proposed a somewhat similar way of differentiating the two contributions [75]. They suggest that the response of conducting carriers completely collapses into a δ-function at $T \ll T_c$. Therefore, the spectrum of $\sigma_1(\omega)$ at $T \ll T_c$ represents the 'midinfrared component' in the conductivity. While this approach appears to be useful under the circumstances and allows one to extract the temperature dependence of the scattering rate below T_c, it also has serious deficiencies. The most significant one stems from the fact that the conductivity in the superconducting state remains finite down to the lowest available frequencies and even increases in a Drude-like fashion at $\omega < 50$ cm^{-1} (figure 8).
[79] Renker B, Gompf F, Gering E, Ewert D, Rietschek H and Dianoux A 1988 *Z. Phys.* B **73** 309
[80] Bourges P, Sidis Y, Regnault L P, Hennion B, Villeneuve R, Collin G, Vettier C, Henry J Y and Marucco J F 1995 *J. Phys. Chem Solids* **56** 1937

[81] Marsiglio F 1996 unpublished
[82] Pines D and Nozières P 1966 *The Theory of Quantum Liquids* (New York: Benjamin)
[83] Bonn D A, Garret J D and Timusk T 1988 *Phys. Rev. Lett.* **61** 1305
[84] Katsufuji T, Kasai M and Tokura Y 1996 *Phys. Rev. Lett.* **76** 126
[85] Tanner D B and Timusk T 1992 *Optical Properties of High-Temperature Superconductors (Physical Properties of High Temperature Superconductors III)* ed D M Ginsberg (Singapore: World Scientific) p 105
[86] Zheng G, Odaguchi T, Mito T, Kitaoka U, Asayama K and Kodama Y 1993 *J. Phys. Soc. Japan* **62** 2591
Ishida K, Kitaoka Y, Ogata N, Kamino T, Asayama K and Cooper J R 1993 *J. Phys. Soc. Japan* **62** 2803
[87] Emery V J and Kivelson S A 1995 *Nature* **374** 434
[88] Kotliar G and Liu J 1988 *Phys. Rev.* B **38** 5142
[89] Rice T M 1992 *The Physics and Chemistry of Oxide Superconductors* ed Y Iye and H Yasuoka (Berlin: Springer) p 313
[90] Fukuyama H 1992 *Prog. Theor. Phys. Suppl.* **108** 287
[91] Lee P A and Nagaosa N 1992 *Phys. Rev.* B **46** 5621
[92] Kampf A P and Schrieffer J R 1990 *Phys. Rev.* B **42** 7967
[93] Barzykin V and Pines D 1995 *Phys. Rev.* B **52** 13 585
[94] Carbotte J P, Jiang C, Basov D N and Timusk T 1995 *Phys. Rev.* B **51** 11 798
[95] Jiang C, Schachinger E, Carbotte J P, Basov D and Timusk T 1996 *Phys. Rev.* B **54** 1264
[96] Quinlan S M, Hirshfeld P J and Scalapino D J 1996 *Phys. Rev.* B **53** 8575
[97] Hardy W N, Bonn D A, Morgan D C, Liang R and Zhang K 1993 *Phys. Rev. Lett.* **70** 3999
[98] Zhang K, Bonn D A, Kamal S, Liang R, Baar D J, Hardy W N, Basov D and Timusk T 1994 *Phys. Rev. Lett.* **73** 2484
[99] Uemura Y J, Luke G M, Sternlieb B J, Brewer J H, Carolan J F, Hardy W N, Kadono R, Kempton J R, Kiefl R F, Kreitzman S R, Mulhern P, Riseman T M, Williams D Ll, Yang B X, Uchida S, Takagi H, Gopalakrishnan J, Sleight A W, Subramanian M A, Chien C L, Cieplak M Z, Xiao G, Lee V Y, Statt B W, Stronach C E, Kossler W J and Yu X H 1989 *Phys. Rev. Lett.* **62** 2317
[100] Uemura Y J, Le L P, Luke G M, Sternlieb B J, Wu W D, Brewer J H, Riseman T M, Seaman C L, Maple M B, Ishikawa M, Hinks D G, Jorgensen J D, Saito G and Yamochi H 1991 *Phys. Rev. Lett.* **66** 2665
[101] Niedermayer C, Bernhard C, Binninger U, Glücker H, Tallon J L, Ansaldo E J and Budnick J I 1993 *Phys. Rev. Lett.* **71** 1764
[102] Gao F, Romero D B, Tanner D B, Talvacchio J and Forrester M G 1993 *Phys. Rev.* B **47** 1036
[103] Startseva T, Hughes R A, Puchkov A V, Basov D N, Timusk T and Mook H A 1996 unpublished
[104] Cooper S L and Gray K E 1994 *Anisotropy and Interlayer Coupling in the High T_c Cuprates (Physical Properties of High Temperature Superconductors IV)* ed D M Ginsberg (Singapore: World Scientific) p 61
[105] Thomas G A, Rapkine D H, Cooper S L, Cheong S-W and Cooper A S 1991 *Phys. Rev. Lett.* **67** 2906
[106] Perkins J D, Kastner M A, Birgeneau R J, Falck J P and Greven M 1993 *Phys. Rev. Lett.* **71** 1621
[107] Kostur V N 1996 *Phys. Rev.* B **53** 2273